

High-Ti inducing local η -phase transformation and creep-twinning in CoNi-based superalloys

Zhida Liang^{1,4*}, Jing Zhang^{2,*}, Li Wang³, Florian Pyczak¹

1. Institute of Materials Physics, Helmholtz-Zentrum Hereon, Max-Planck-Strasse 1, Geesthacht 21502, Germany
2. Key Laboratory of MEMS of Ministry of Education, School of Integrated Circuits, Southeast University, Nanjing, China
3. State Key Laboratory of Powder Metallurgy, Central South university, 410083 Changsha, China
4. Laboratory for Electron Microscopy, Karlsruhe Institute of Technology, Engesserstraße 7, Karlsruhe 76131, Germany

*Corresponding author: zhida.liang@outlook.com (Zhida Liang), jizh@seu.edu.cn (Jing Zhang)

Abstract

Precipitate shearing mechanisms during compressive creep of $L1_2$ -containing CoNi-base alloys with different Ti/Al ratio have been investigated in this work. Interrupted creep tests were conducted at 950 °C under air with constant load stress of 241 MPa. It was found that the creep resistance increases with Ti/Al ratio rising in CoNi-based alloys. In addition, we firstly found that the type of planar defects on (111) planes during precipitate shearing change from antiphase boundary (APB) towards superlattice extrinsic stacking fault (SESF) with Ti content increasing - shearing of the γ' phase is mainly dominated by APB in Ti-free and low-Ti alloys but dominated by SESF in high-Ti alloys. By employing density functional theory (DFT), the APB energy was found be lower than complex stacking fault (CSF) energy in Ti-free and low-Ti alloys but this situation becomes opposite in high-Ti containing alloys. Additionally, the SESF energy is lower than SISF energy in $L1_2$ -(Co,Ni)₃Ti structure strongly supporting SESFs formation in high-Ti alloys. By energy dispersive X-ray spectroscopy analysis under the scanning transmission electron microscope mode, the observed chemical segregation enables APB becoming disordered γ phase structure in Ti-free and low-Ti alloys and enables SESF becoming local ordered η phase structure in high-Ti alloys. However, the microtwins were found as well in high-Ti alloys which usually contributes higher creep strain than other planar defects, e.g. SESF and APB. This finding provides a new insight how to use Ti content reasonably in superalloy design.

Keywords: Superalloys, Transmission electron microscopy, First-principles calculations, Twinning, Phase transformation

1. Introduction

The high-temperature creep resistance of superalloys results from the high content of the coherent ordered precipitates to resist dislocation gliding and shearing [1]. During creep, the accumulated stresses in the precipitates ultimately rise to levels high enough to cause shearing. Over the years, extensive experimental, theoretical and numerical studies have been dedicated to understanding its intrinsic properties of the dislocation shearing in the γ' precipitates of superalloys [2-10]. Depending on the discrepancy of alloys' composition, applied stress and testing temperature, a variety of different γ' precipitate shearing modes become operative [6]. Generally, at lower stresses and higher temperatures, shearing of the γ' precipitates in Ni based and CoNi based superalloys, is governed by the movement of paired $a/2\langle 1\ 1\ 0\rangle$ dislocations with leaving an antiphase boundary (APB) in their wake [4]. However, shearing of a γ' precipitate in Co-based superalloys is caused by sliding of a single $a/3\langle 112\rangle$ super-Shockley partial combining with the formation of but leaving a superlattice intrinsic stacking faults (SISF) [11, 12].

Usually, at intermediate temperatures, in the range of 600 and 850 °C, reorder-mediated γ' precipitate shearing modes, including superlattice stacking faults (SSF) and deformation twinning, become prevalent during creep [5, 6]. During creep deformation, a paired $a/2[011]$ dislocations dissociate during shearing the γ' phase, leading to a high-energy faulted structure (the so-called complex stacking fault, CSF), which is further transformed into superlattice extrinsic stacking faults (SESF) by diffusion-mediated atomic reordering to eliminate the high energy unfavourable Al-Al first nearest neighbour bonds.

The SESFs were consider as 'embryo' for the formation of creep microtwin [5]. Smith *et.al.* [10, 13] proposed that chemical segregation induces local phase transformation (LPT) causing weakening or strengthening. The segregation of additional elements, Ti, Ta, Hf, and Nb, leads to a potent LPT strengthening effect by formation of η ($D0_{24}$) along SESFs. For instance, in the Ni-base superalloys ME03 and ME501, Cr, Mo and W were found to segregate to SESFs ($Co_3(Cr,Mo,W)$, χ phase) and to result in LPT weakening in the low Nb+Ta content alloy ME03, while Nb and Ta segregation to SESFs ($(Co,Ni)_3(Ti,Nb,Ta)$, η phase) results in LPT strengthening in the high Nb+Ta content alloy ME501. In the density functional theory (DFT) calculations [10], it was predicted that the segregation of η phase formers (Nb, Ta and Ti) will lead to transformation of the SESF towards hcp η phase, which promote stability of SESFs and inhibits the deleterious thickening of SESFs towards the formation of microtwins. Conversely, if the γ phase formers, *e.g.* Co, Cr and Mo, segregate to the SESFs which indicates the faults transform to a γ -like region. The Shockley partials are able to shear the γ' precipitate along the SESF with little energy penalty, promoting nanotwin formation. Liliensten *et.al* [14] summarized the local transformation

tendency to ordered, hard, geometrically closed packed (GCP) phases of the Ni_3X type, especially at SESFs. Ta and Nb are more potent GCP stabilizers than Ti, hence a potency weight factor of 0.5 was assigned to the Ti content. When the $(Nb + 0.5Ti + Ta)/Al$ ratio exceeds ~ 0.625 , a local η -phase formation at the SESF will occur. Although the effects of Nb and Ta on phase transformation has already been reported by a number of publications [10, 13, 14], to authors' best knowledge, the studies regarding the effect of Ti on phase transformation and creep twinning are rather limited. On the other hand, there is no direct evidence for "bulk" η phase formation in CoNi based superalloys yet.

In this study, the planar fault transformation (APB \rightarrow SESF), as a result of changing Ti/Al ratios in CoNi based superalloys, was firstly unveiled under low stress at high temperature of 950 °C. The potential APB \rightarrow SESF transformation mechanism was explained by the DFT calculation. The chemical segregation at planar faults was analysed using energy dispersive X-ray spectroscopy (EDS) in scanning transmission electron microscopy (STEM). The local η phase formation triggered by Ti, Mo and W segregation is firstly discovered in CoNi-based superalloys at 950 °C. Additionally, we found direct evidence for 'bulk' η phase at microscale in alloys with high Ti/Al ratios which is a strong hint for $\gamma'\rightarrow\eta$ displacive-diffusive phase transformation. The details of the mechanisms related to the local phase transformation (LPT) are proposed and their influence on the overall mechanical behaviour of the alloy is discussed. This work provides a deep insight into precipitate shearing mechanisms, which is critical for designing more robust superalloys in the future.

2. Experiments and Methods

2.1 Materials

The alloys under investigation are γ' -phase hardened polycrystalline CoNi-based superalloys named 0Ti, 2Ti, 4Ti, 6Ti, 8Ti, 10Ti and 12.5Ti with the nominal chemical composition Co-30Ni-(12.5-x)Al-xTi-2.5Mo-2.5W (x= 0, 4, 8, 10 and 12.5 at.%). The average alloy composition was measured by SEM-EDS and is shown in **Table 1**. The alloys were melted at least 7 times under argon in the form of a 70 g ingot button on a water-cooled copper hearth using a laboratory-scale vacuum arc melting unit. The as-cast material was homogenized at 1250 °C for 24 h. In addition, alloys 0Ti, 4Ti and 8Ti with extra 0.1% B were melted again and then homogenized followed by ageing at 900 °C in air for 220 h, and subsequently air cooled to room temperature. The resultant images of γ'/γ binary phases in alloys 0Ti, 4Ti and 8Ti with extra 0.1% B were shown **Fig. S1**.

Table 1. Average alloy composition in atomic percent by SEM-EDS.

Alloys	Co	$\pm\sigma$	Ni	$\pm\sigma$	Al	$\pm\sigma$	Ti	$\pm\sigma$	Mo	$\pm\sigma$	W	$\pm\sigma$
0Ti	53.2	0.14	30.2	0.04	11.6	0.06	–	–	2.4	0.04	2.6	0.03
2Ti	53.3	0.11	29.8	0.06	9.8	0.11	2.0	0.03	2.5	0.03	2.6	0.03
4Ti	52.8	0.22	30.3	0.27	7.8	0.07	4.1	0.13	2.4	0.09	2.6	0.06
6Ti	53.0	0.11	30.1	0.09	6.0	0.05	5.9	0.01	2.4	0.04	2.6	0.05
8Ti	52.6	0.30	30.1	0.23	4.2	0.16	8.1	0.07	2.4	0.02	2.5	0.07
10Ti	52.7	0.07	30.0	0.03	2.2	0.03	10.1	0.09	2.4	0.1	2.6	0.07
12.5Ti	52.3	0.10	29.9	0.18	–	–	12.7	0.18	2.4	0.08	2.6	0.03

2.2 Creep testing

Compression creep tests of the alloys with extra 0.1% B were performed using a Satec Systems constant load machine with a lever arm ratio of 16:1. The creep tests in alloys 0Ti, 4Ti and 8Ti were performed in air, at 950 °C with compressive stresses of 241MPa. The creep tests were stopped manually after creep strain of 4.0 %.

2.3 Microstructural characterization

The γ/γ' two-phase microstructures of the aged samples were characterized by backscattered electron (BSE) imaging in a scanning electron microscope (FE-SEM, Zeiss, Germany Gemini). A CMOS EBSD Detectors with AZteclive analysis software was used for Electron Backscatter Diffraction (EBSD) measurements.

For transmission electron microscopy (TEM) sample preparation, 3 mm disks were mechanically polished to a thickness of about 75 μm . The final samples were thinned to electron transparency by a twin jet electro polishing unit using the Struers A3 electrolyte with a voltage of 32 V at -38 °C. High resolution high angle annular dark field (HAADF) imaging was performed in a Thermo Fisher Scientific Themis Z operated at 300 kV with a probe-corrector to investigate the structure of defects in atomic resolution. The Thermo Fisher Scientific Talos 200i equipped with a Super-X Energy Dispersive X-ray Spectroscopy (EDS) detector was employed to analyze the local chemical composition around defects.

2.4 First-principles calculations

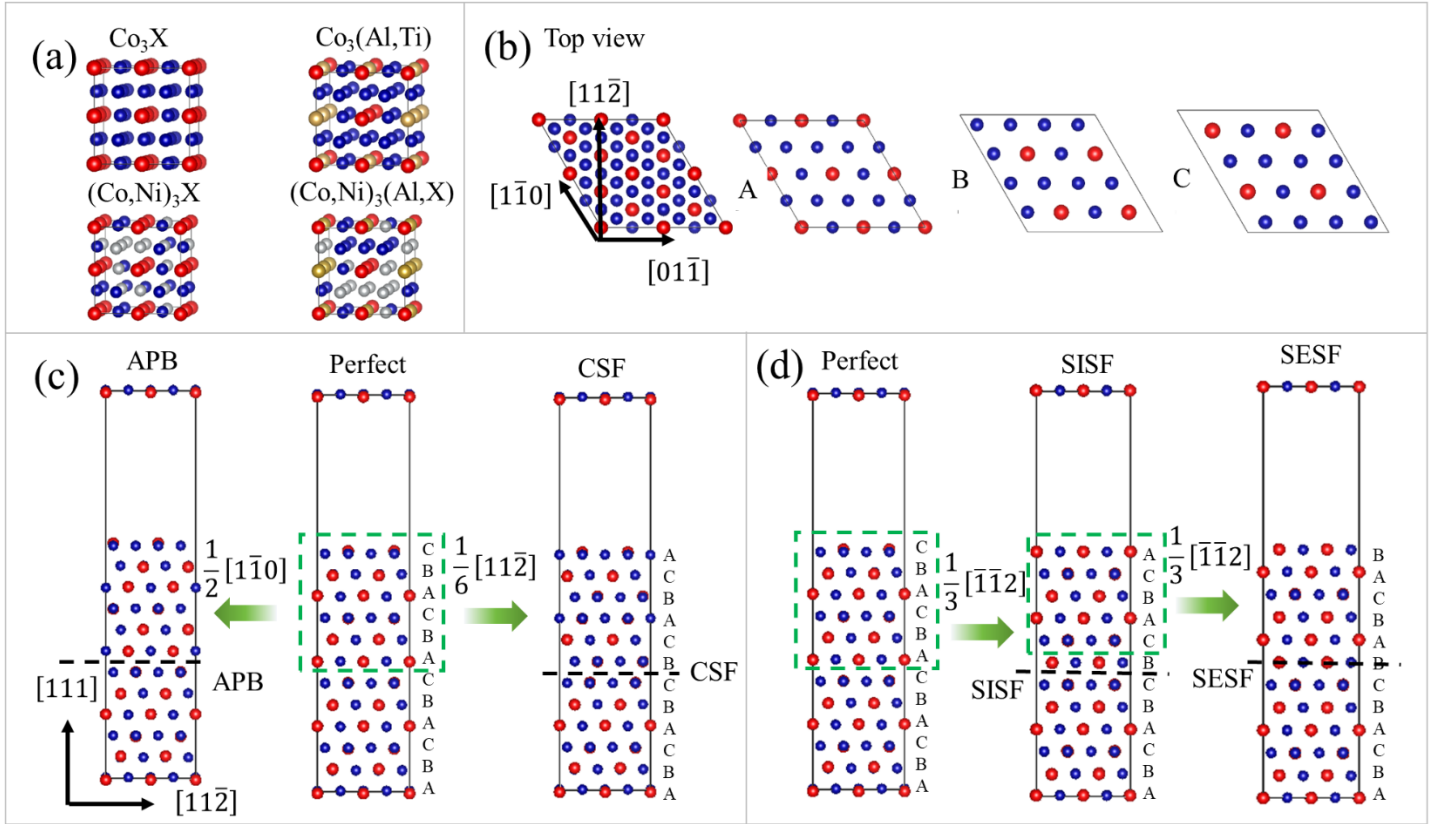


Fig. 1. Supercell models of first-principles calculations. (a) supercell models of bulk optimization for binary, ternary and quaternary L_{12} -Co-based phases; (b) top view of stacking fault supercells with atomic distributions of A, B and C layers; (c) generation of APB and CSF through planar shearing; (d) generation of SISF and SESF through planar shearing along $[\bar{1}\bar{1}2]$ direction.

The calculations of planar defects were performed based on the Density Functional Theory (DFT) and Projector Augmented Wave (PAW) [15] method implemented in the Vienna Ab-initio Simulation Package (VASP) [16]. The Special Quasi-random Structures (SQS) [17] method was applied to treat the random distribution of different atomic species on the two sublattices in the L_{12} structure. The generalized gradient approximation parameterized by Perdew-Burke-Ernzerhof (PBE) [18] was adopted to describe the exchange-correlation functional. The cutoff energy of the wave function expansion was set to 450 eV. The convergence criterion of energy and force are 10^{-6} eV/cell and 10^{-3} eV/Å for geometry optimizations. $2 \times 2 \times 2$ supercell models consisting of 32 atoms were applied in the bulk optimization of Co-based alloys, as **Fig.1(a)** displays. After the bulk optimization, a supercell model to generate planar stacking faults was constructed, which contains twelve (111) layers and a total of 192 atoms, with the lattice vectors a , b and c being along $[\bar{1}\bar{1}0]$, $[0\bar{1}\bar{1}]$ and $[111]$ directions, as shown in **Fig. 1(b)**. A 15 Å

vacuum layer was added to the supercell model of stacking fault in order to eliminate the periodic effect. $11 \times 11 \times 11$ and $3 \times 3 \times 1$ Monkhorst-Pack [19] grids of k-points were used in the integration over the Brillouin zone during the bulk optimizations and calculations of planar defects, respectively.

In the calculations of SFEs, the perfect supercell model, as **Fig.1(c)** shows, was optimized with full relaxation of atomic positions. Then, the APB was generated by shifting the upper six layers along a $\frac{1}{2}[01\bar{1}]$ vector relative to the lower six layers, as indicated in **Fig. 1(c)**. Similarly, the CSF was obtained by shearing a $\frac{1}{6}[11\bar{2}]$ displacement vector. When applying a $\frac{1}{3}[\bar{1}\bar{1}2]$ shear displacement vector to the upper six layers, the planar fault of SISF can be created, as illustrated in **Fig.1(d)**. Subsequently, based on the SISF model, the SESF was obtained by shifting the top five layers with a $\frac{1}{3}[\bar{1}\bar{1}2]$ vector. During the calculations of planar defects, the relaxation of atomic positions along the x and y directions was fixed.

3 Results

3.1 Creep tests and deformation structure analysis by STEM

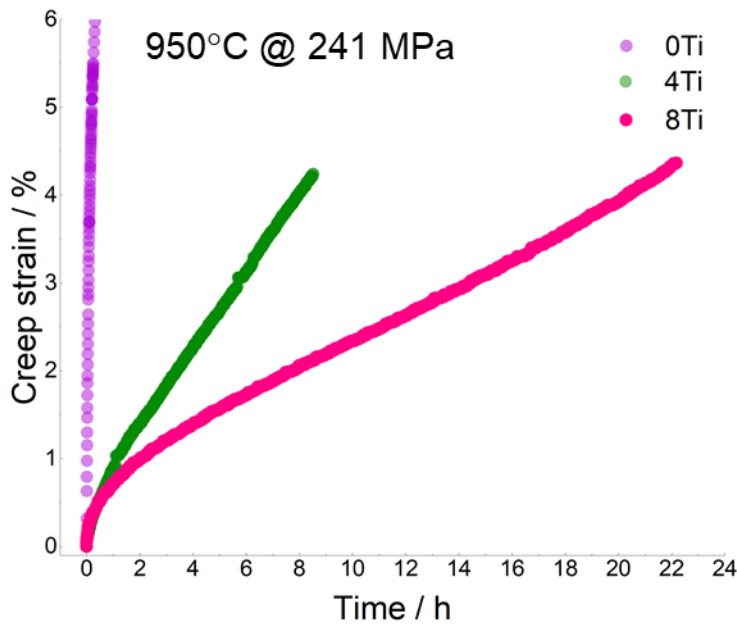


Fig. 2. Compression creep test of alloys 0Ti, 4Ti and 8Ti at 950 °C with applied stress of 241 MPa.

Fig. 2 presents the creep test results of alloys 0Ti, 4Ti and 8Ti at 950 °C with an applied stress of 241 MPa. The high-Ti alloy (8Ti) exhibits much higher creep resistance than the low-Ti (4Ti) and Ti-free (0Ti) alloys. The creep

process is usually diffusion rate-controlled but the alloys 0Ti, 4Ti and 8Ti contain the same amount of slow diffusion elements Mo and W. Elements diffusion should not be a good excuse to explain the discrepancy for creep performance in the alloys 0Ti, 4Ti and 8Ti. We think the improved creep resistance can be attributed to the high Ti/Al ratio in alloys. For instance, high Ti/Al ratio can bring the alloys higher volume fraction of the γ' precipitates, higher γ'/γ lattice misfit and stronger γ' precipitates with higher APB energy [20]. H. Harada et.al. [21, 22] concluded that the creep resistance is better in alloys with higher volume fraction of γ' precipitates when this value is lower than 65 %. In addition, the induced higher γ'/γ lattice misfit will bring more dense dislocation network which enhances creep resistance directly, as evidenced by a serial of literature studies [23, 24]. These factors together determine that higher Ti/Al ratio alloys can obtain more excellent creep resistance.

The resultant post-mortem SEM-BSE images for compression creep test of alloys 0Ti, 4Ti and 8Ti are shown in **Fig. 3(a)**. After creep deformation, the γ' particles in alloy 0Ti become irregular while directional coarsening (rafting) appears in alloys 4Ti and 8Ti. Additionally, we found creep microtwins formed in alloy 8Ti. To get a more detailed insight into the microstructure of the crept specimens, the HAADF-STEM was employed to image defects, including dislocation networks and planar faults (SESF and APBs), near the [011] zone axis. In alloy 0Ti, no dislocation networks were observed. However, a number of planar faults, *i.e.* APBs, were identified in the γ' precipitates, which suggests that a significant of dislocations tend to shear the γ' precipitates by sliding instead of overcoming then by climb along the interface of the γ and γ' phases. In contrast, there are dense dislocation networks formed along the interface between the γ'/γ phases in alloys 4Ti and 8Ti, but the γ' precipitate shearing mode changed from APBs to SESFs with Ti concentration increasing from 4 at.% to 8 at.%.

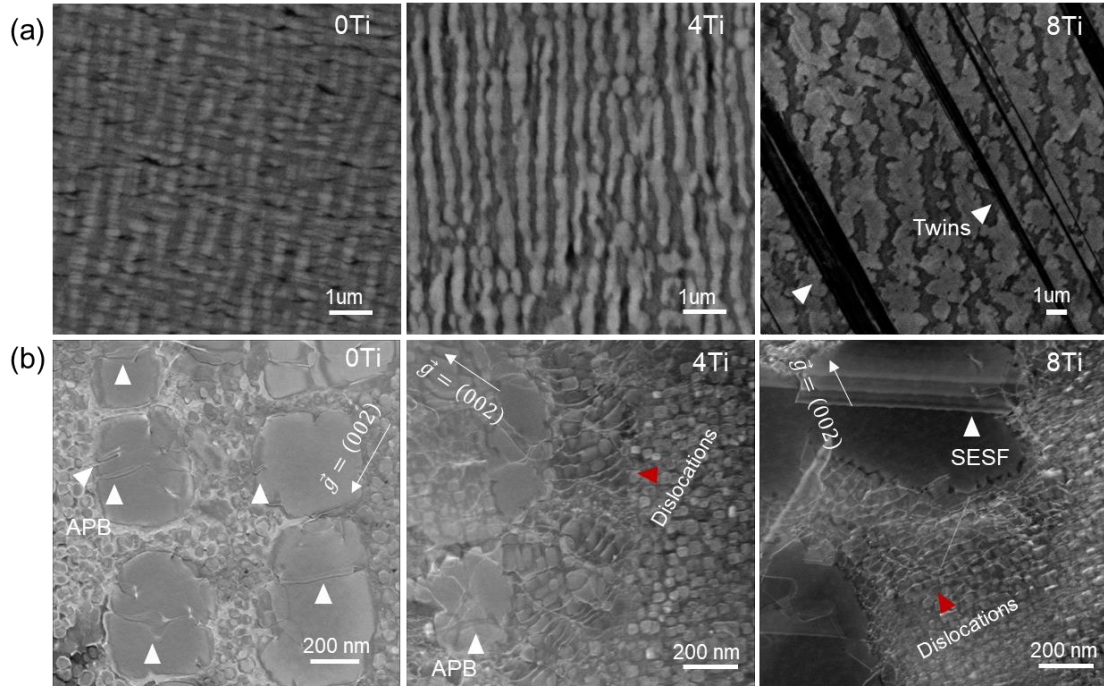


Fig. 3. (a) Post-mortem SEM-BSE images for compressive creep specimens of alloys 0Ti, 4Ti and 8Ti. (b) HAADF-STEM (0Ti, 4Ti and 8Ti) images of dislocation networks and planar defects (SESF and APBs) taken near the [110] zone axis. (The white arrows indicate planar defects and red arrows indicate dislocation networks.)

3.2 Creep twinning in alloy 8Ti

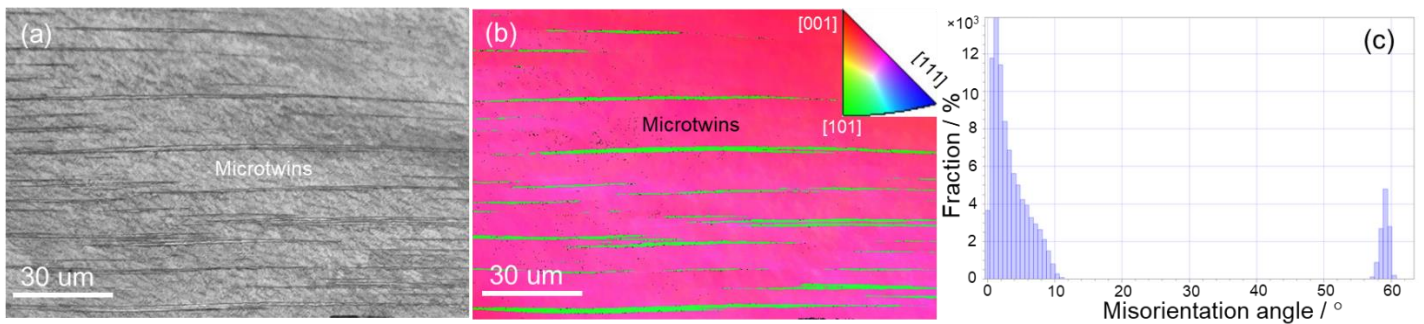


Fig. 4. Creep twinning identification by EBSD in the crept specimen of alloys 8Ti. (a) Pattern quality map, (b) Inverse pole figure (IPF) map and (c) Misorientation distribution of IPF in (b).

To confirm that the structures found in **Fig. 3(a)** are indeed creep twins in alloy 8Ti, we did EBSD measurement. **Fig. 4(a)** and **(b)** present the Kikuchi pattern quality map and the related inverse pole figure (IPF) map from the same region. The features, highlighted as green color, appear to have a typical $\Sigma 3$ twin relationship with the surroundings, which is also evident from the misorientation angle distributions, shown in **Fig. 4(c)**.

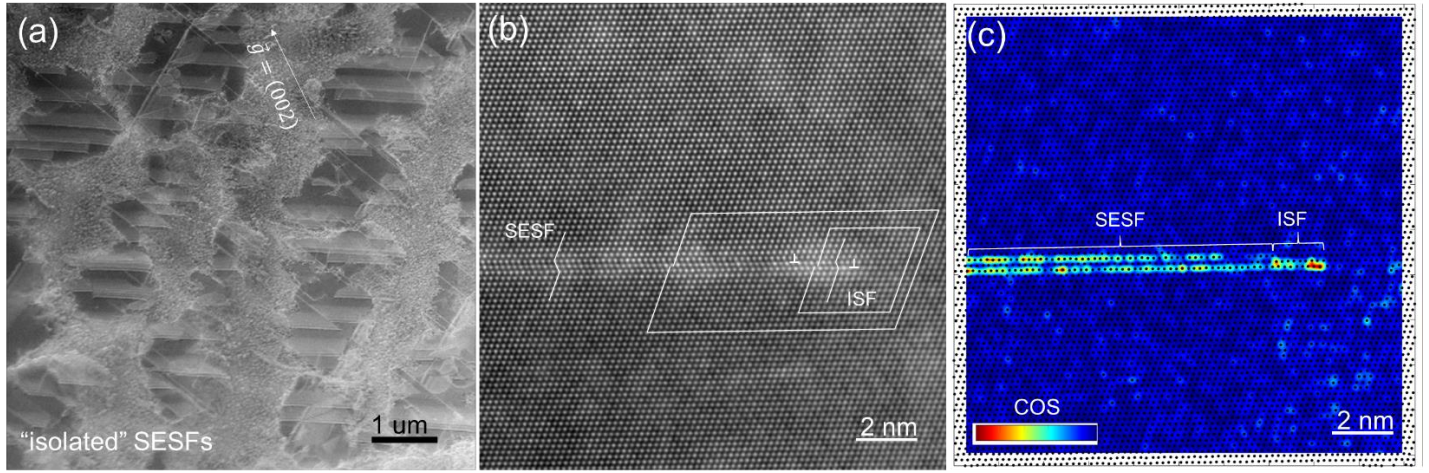


Fig. 5. (a) HAADF-STEM image of ‘isolated’ SESFs taken near the [110] zone axis in alloy 8Ti. (b) HRSTEM micrograph showing an SESF terminating in an ISF. (c) Center of symmetry (COS) visualization of the area highlighting the deviations from crystal symmetry produced by the stacking fault in **Fig. 5(b)**.

The majority of the observed shearing events are isolated SFs inside the γ' precipitates in alloy 8Ti, as shown in **Fig. 5(a)**. According to the well-established criteria for distinguishing between extrinsic and intrinsic SF types, see **Fig. S2**, the \vec{g} vector points away from the outermost bright fringe of the stacking faults. Therefore, the isolated SFs were identified as extrinsic SFs. **Fig. 5 (b)** presents the atomic HAADF-STEM image of a SESF which terminates in an ISF. The one-layer fault ISF is in the lead, then transitions to the two-layer fault ESF. The high enhanced Z-contrast in the fault region hints the segregation of high atomic number elements, e.g., Mo and W. Following the finish-to-start right-hand (FS/RH) convention, a Burgers circuit around leading partial dislocation yields the projection Burgers vector $\vec{b}_p = \frac{a}{12} [\bar{1}12]$ into the (110) image plane, with the line direction $\vec{u} = k[110]$ ($k = 1/4$) perpendicular to the (110) image plane. Therefore, the Burgers vector of this Shockley partial dislocation is $\vec{b} = \frac{a}{6} [121]$. Since the leading partial is a $1/6\langle 121 \rangle$ partial, nearest neighbor violations must be created in their wake, necessitating a re-ordering process in order to form a true SESF. Likewise, the transition from a CISF to an SESF was considered as a verification of local re-ordering as proposed by the Kolbe mechanism [25]. Karpstein et.al [26] described a similar defect configuration and unambiguously experimentally demonstrated the nature of the two segments being two clear Shockley partial dislocations.

The Kolbe mechanism considered two $\langle 110 \rangle$ dislocations interacting in the γ matrix in such a way that two Shockley superpartial dislocations are created according to

$$\begin{cases} \frac{1}{2}[\bar{1}10] \rightarrow \frac{1}{6}[\bar{1}2\bar{1}] + \frac{1}{6}[\bar{2}11] \\ \frac{1}{2}[\bar{1}01] \rightarrow \frac{1}{6}[\bar{1}\bar{1}2] + \frac{1}{6}[\bar{2}11] \end{cases}$$

leading to partials of highest Schmid factor for compression along $\langle 110 \rangle$ which are able to shear the precipitate.

This results in the formation of a two-layer CSF, whereby the segregation of element to this fault reduces the high energy penalty by transforming it into a lower energy stacking fault. In this work, the finding of two Shockley partial dislocations follows the Kolbe mechanism. The formation of a SESF can take place by the dissociation of two $\langle 110 \rangle$ dislocations. However, the single leading $a/6 \langle 121 \rangle$ partial dislocation propagation into the γ' precipitates has been observed during creep of an $L1_2$ hardened polycrystalline Co-based superalloy at an intermediate temperature of 760 °C, where these faults extend and thicken into micro-twins [27]. In our opinion, the Kolbe mechanism is one of the possible pathways for SESF formation.

3.3 Chemical fluctuations at planar faults of APB and SESF

The chemical fluctuations in the vicinity planar faults apparently become one important feature during creep deformation in superalloys. **Fig. 6** presents the HAADF image and elemental maps illustrating the chemical fluctuation around an APB on a (111) plane inside a γ' precipitate in alloy 0Ti. The elemental maps (**d-h**) reveal the segregation of Co at the APB₍₁₁₁₎ with a corresponding depletion of Ni, Al, Mo and W. An integrated line scan of the area in the composite chemical map is shown in **Fig. 6(i)** and **(j)**. The quantified line scan further confirms the presence of Co segregation at the APB₍₁₁₁₎, as well as, depletion of Ni, Al, Mo and W. Based on the EDS maps, the element Co also segregated and Ni, Al, Mo and W depleted at the leading dislocation (terminating the APB in the γ' precipitate) which is in a similar manner to the APB region.

A number of publications [2, 28, 29] have reported the disorder structure of APBs on (111) planes in the γ' phase by using high resolution STEM. A deeper insight into local chemistry of planar faults was obtained by aberration-corrected high-resolution STEM and the advanced capabilities of EDS. The residual ordering contrast was observed along the full length of the APB. This observation indicated that the crystal lattice in the broadened APBs still retains a certain degree of $L1_2$ atomic ordering, even though the chemical composition approaches that of the disordered γ phase. Yet, He et.al. [28] and Lu et.al [29] investigated Fast-Fourier-transform (FFT) patterns along [110] zone axis from APB region on (111) planes region and superlattice diffraction spots disappear in the FFT pattern from the APB region that indicates these regions have formed a fully disordered γ phase structure.

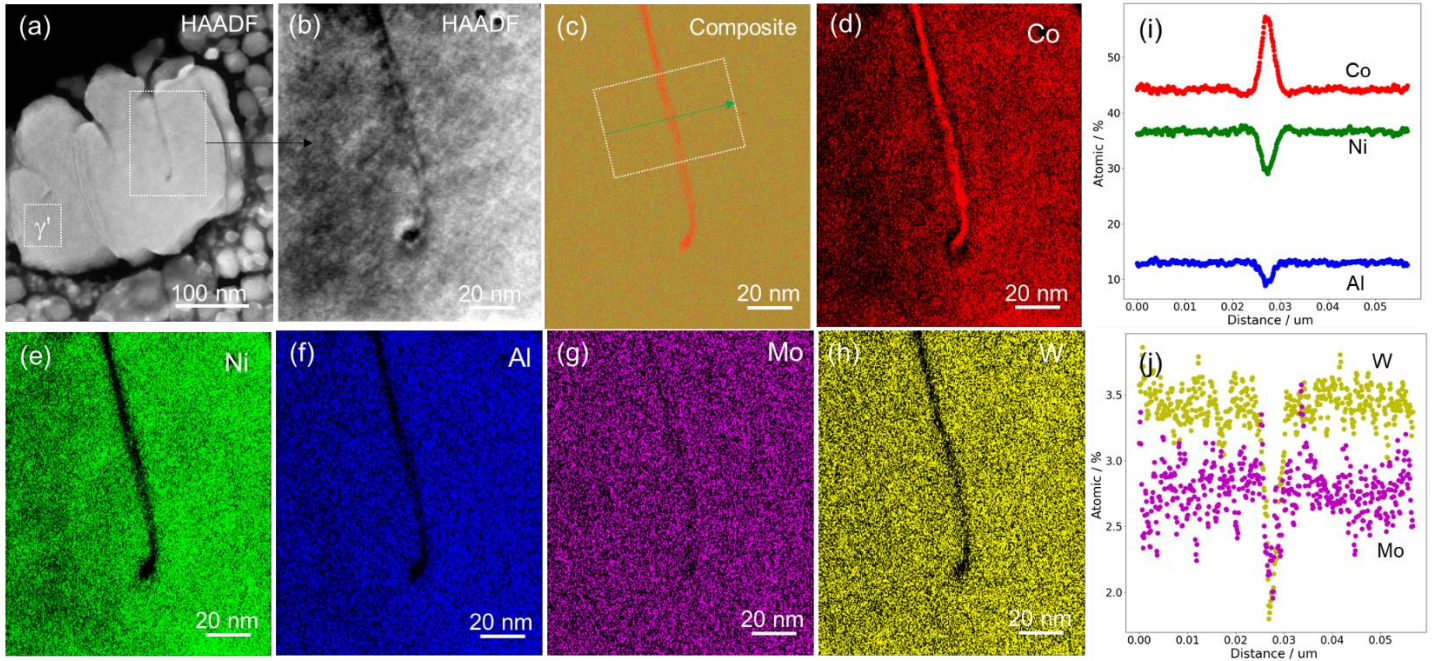


Fig. 6. Chemical fluctuations analysis around an APB region on a (111) plane in alloy 0Ti. (a) HAADF-STEM image of the γ' precipitate with APBs taken along [011] beam direction. (b) Magnified image of white rectangular marked in (a). (c) Composite chemical map of elements Co, Ni, Al, Mo and W. (d)-(h) Net intensity elemental maps of elements Co, Ni, Al, Mo and W. (i) and (j) EDS line scan integrated along the APB in the region marked in (c).

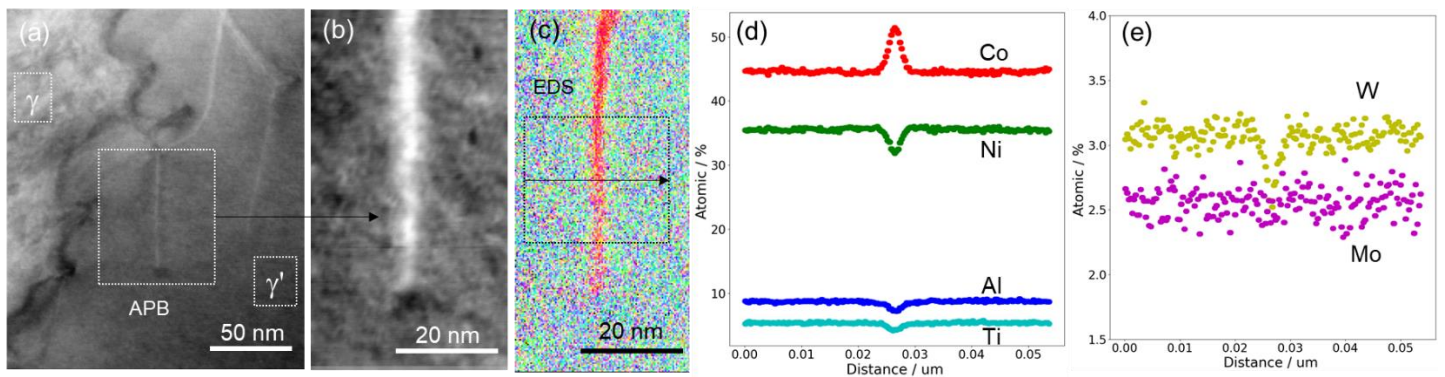


Fig. 7. Chemical fluctuations analysis around an APB region on a (001) plane in alloy 4Ti. (a) HAADF-STEM image of the γ' precipitate with an APB taken along [001] beam direction. (b) Magnified image of white rectangular marked in (a). (c) Composite chemical map of elements Co, Ni, Al, Ti, Mo and W. (d) and (e) EDS line scan integrated along the APB in the region marked in (c).

Fig. 7 shows the HAADF images ((a) and (b)) and a chemical composite map (**Fig.7 (c)**) of the region around an APB siting on a (001) plane inside a γ' precipitate in alloy 4Ti. An integrated line scan of the area represented in the composite chemical map is presented in **Fig. 7(d)** and (e). The quantified line scan confirms the presence of Co segregation along the APB₍₀₀₁₎, as well as, depletion of Ni, Al, Ti and W. In **Fig. S3**, the element segregation results around APB region on (111) planes are same to APB region on (100) planes which indicates full disordered γ phase structure occurred along APB region on (001) and (111) planes.

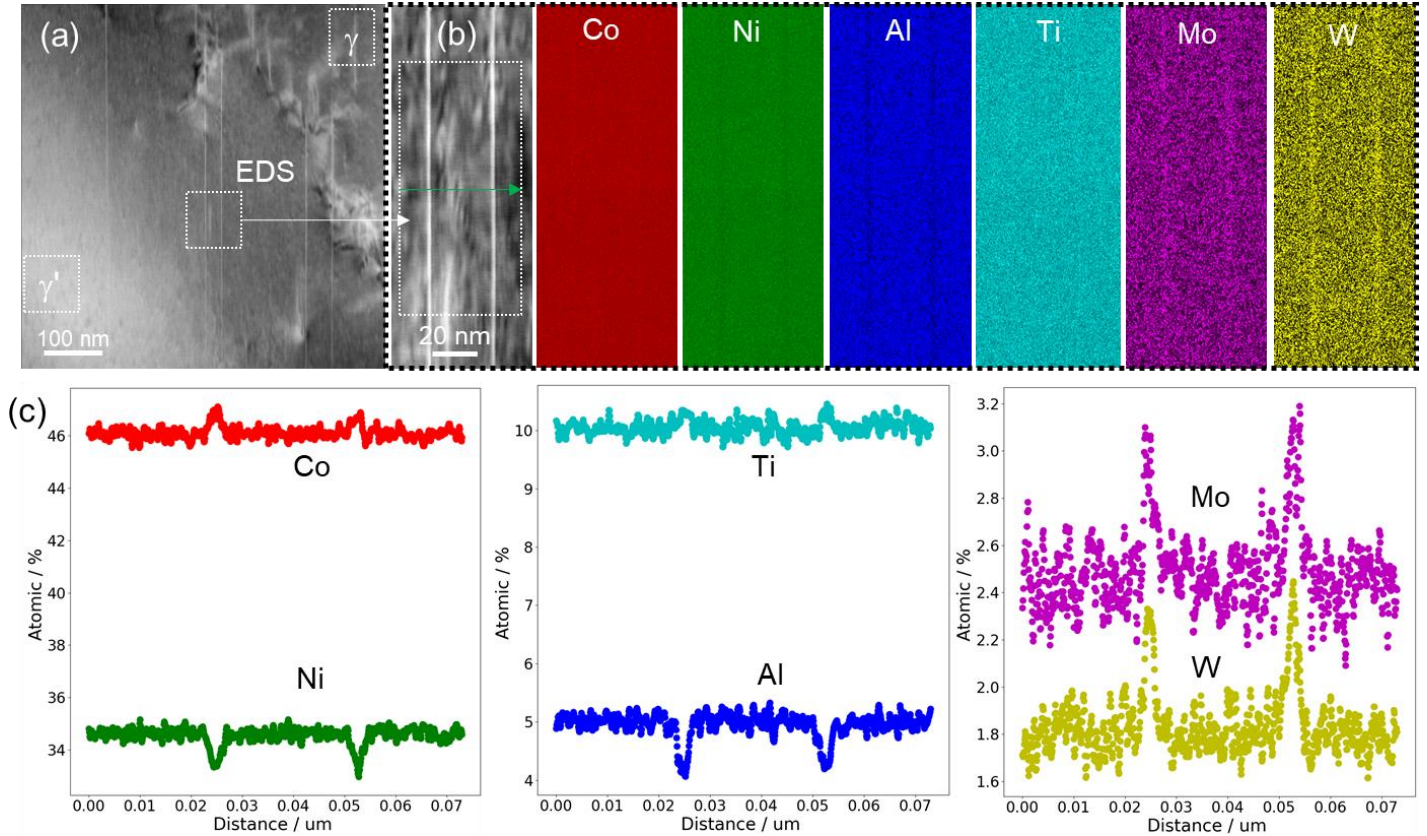


Fig. 8. Chemical fluctuations analysis in alloy 8Ti. (a) HAADF-STEM image of SESFs in [011] beam direction. (b) Net intensity elemental maps of two vertical SESFs. (c) The integrated EDS line scanning curves represent the area incorporated into the vertically integrated line scan shown from (b).

The element partition between γ and γ' phase in alloys 0Ti, 4Ti and 8Ti was also analyzed by STEM-EDS and the results are shown in **Fig. S4**. In alloy 0Ti, only Co prefers to partition into the γ matrix while Ni, Al, Mo and W partition into the γ' phase. In alloy 4Ti, Co prefers to partition into the γ matrix as well and Ni, Al, Ti and W partition into the γ' phase but Mo has a balanced distribution in the γ' and γ two phases. In alloy 8Ti, Co and Mo prefer to partition into the γ matrix and Ni, Al, Ti and W partition into the γ' phase. With increasing Ti content in

CoNi-based superalloys, the partitioning tendency of Mo changes from γ' phase former to γ phase former. Element partitioning towards to the γ matrix phase of alloys 0Ti and 4Ti is same to segregation tendency at APB regions inside the γ' precipitates. Therefore, in terms of chemical composition analysis, the APB inside a γ' precipitate is represents an indeed a localized disordered γ phase region.

Fig. 8(a) shows a low-magnification HAADF-STEM image of several SESFs from shearing events inside a γ' precipitate. The elemental maps **Fig. 8(b)** reveal segregation of Co, Mo and W along the SESF with a corresponding depletion of Ni and Al. An integrated line scan of the area represented in the HAADF-STEM image is presented in **Fig. 8(c)**. The quantified line scan confirms the enrichment of Co, Mo, W and to a slight degree Ti along the SESF, as well as, depletion of Ni and Al. In addition, a Co-rich Cottrell atmosphere exists around the leading shearing Shockley partial configurations, see **Fig. S5**. Based on DFT calculations in literature [13], Nb and Ta have stronger segregation tendencies towards SESFs than W and Mo but it is also indicated that a segregation of W and Mo at SESFs is energetically favorable.

3.4. The γ' to η phase transformations

In order to further confirm that the element segregation tendencies at SESFs lead to a LPT, we carried out a long-term aging heat treatment (1036 h at 900 °C) for 8Ti alloys. During this long-term heat treatment, the bright lath η phases formed at grain boundaries, see **Fig.9** (a). The formation of a $D0_{24}$ lath-like structure may be similar to a Widmanstätten phase transformation of a type $L1_2 \rightarrow D0_{24}$, with the possible HCP habit planes form in cubic matrix. The lath-like η phase' composition was measured by SEM-EDS as well as chemical composition of the γ' phase, SESFs and bulk η phase in alloy 8Ti was compared, as shown in **Fig. 9(b) and Table 2**. Compared with the γ' phase, a simultaneous enhancement in Co, Ti, Mo and W content and a decrease in Ni and Al content is found in the η lath and at SESF faults. The equilibrium composition of SESFs in a γ' precipitate is not identical to the equilibrium composition of the bulk $(Co,Ni)_3(Ti,Mo,W)$ phase of the same crystal structure. However, from γ' phase to SESFs to bulk η phases, there is a composition variation trend, i.e., the content of elements Co, Ti, Mo and W increased and the one of Ni and Al decreases in parallel. The difference in equilibrium compositions between the SESF and the thicker baths of $(Co,Ni)_3(Ti,Mo,W)-D0_{24}$ is perhaps not surprising when considering that the SESF is only 5 atomic layers thick and is not a bulk phase. Beside of this, the SESF formed during creep deformation while the η lath formed from the decomposition of the γ' precipitate during long term aging.

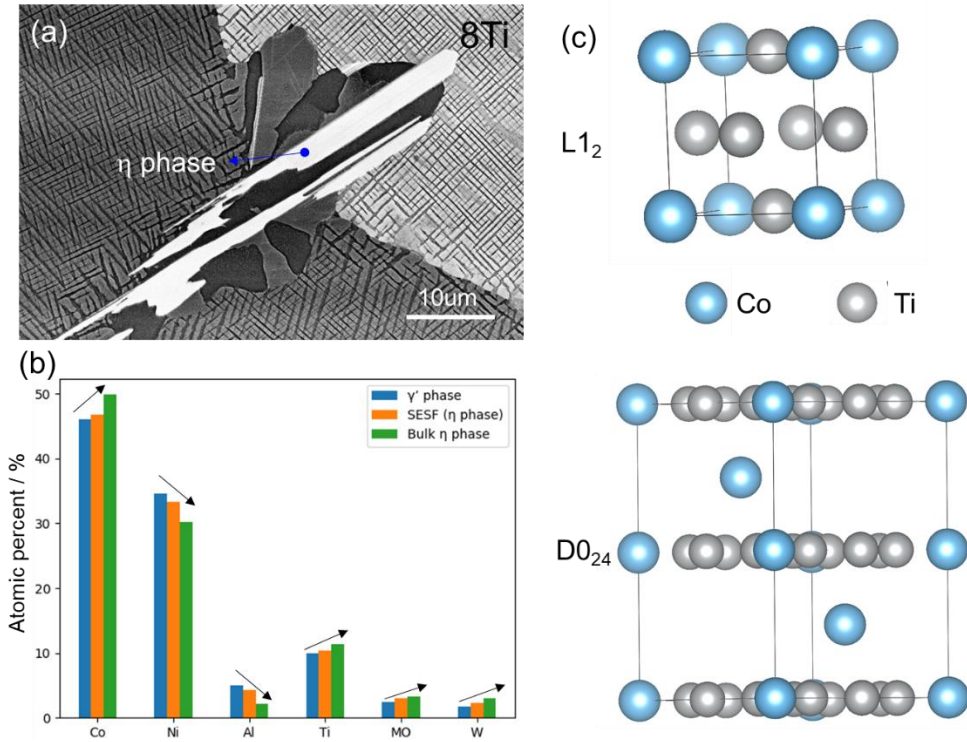


Fig.9 (a) SEM-BSE image with the coarse lath-like η phase in alloy 8Ti after 1036 h aging heat treatment at 900 °C. (b) Compositions (at.%) comparison of the γ' phase, SESF region (local η phase) and lath η phase. (The composition details were shown in **Table 2**.)

To further provide solid evidence regarding the intimate relationship of high Ti content and η phase formation, we prepared 7 alloys with different Ti/Al ratios by using Ti to substitute Al in alloys of Co-30Ni-(12.5-x)Al-xTi-2.5Mo-2.5W (at.%) composition. **Fig.10** presents SEM-BSE images of those alloys with enlarged inserts showing γ/γ' phase microstructures. If the Ti content is higher than 8 at.%, we can clearly see the more bulk η phases formed which were identified by EBSD technique, see **Fig.10(f), (g)** and **(h)**. The crystallographic information for the prototype η phase (Ni₃Ti or Co₃Ti) is shown in **Table S1**.

Table 2. Compositions (at.%) of the γ' phase and SESF (η phase) measured by STEM-EDS and bulk η phase measured by SEM-EDS, respectively.

Elements	Co	Ni	Al	Ti	Mo	W
γ' phase	46.10	34.64	5.01	10.00	2.49	1.75
SESF (η)	46.82	33.26	4.22	10.36	2.97	2.36
Bulk η phase	49.86	30.26	2.17	11.38	3.31	3.02

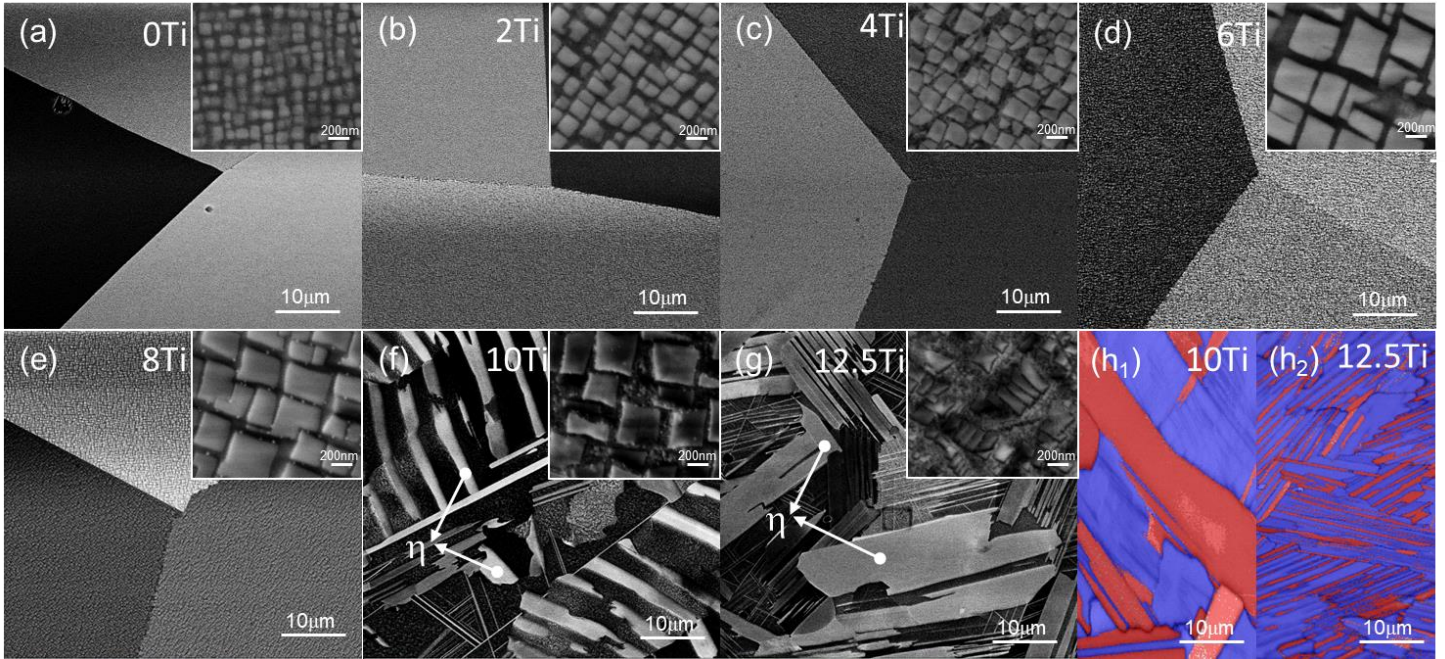


Fig.10 SEM-BSE images (a-g) and EBSD images (h₁ and h₂) of alloys 0Ti, 2Ti, 4Ti, 6Ti, 8Ti, 10Ti and 12.5Ti after homogenization heat treatment at 1250 °C. (In the EBSD images, the red phases are the η phases and the blue phases are the mixed γ and γ' phases.)

4 Discussion

In the present study, we demonstrated that different types of planar faults are formed during creep deformation depending of the Ti content, i.e., with low Ti content APBs form but SESFs form with high Ti content in CoNi-based superalloys. We will discuss the discrepancy of APB and CSF energies with different Ti concentration in L1₂ structure to prove the type of planar fault formation during deformation. In addition, the γ' to η phase transformations in CoNi based superalloys with high-Ti will be discussed in details.

4.1 Planar faults and their formation energies

Shearing mechanisms of γ' precipitates in Co, CoNi and Ni based superalloys have been extensively investigated over a broad range of temperatures [1-5, 24, 25]. Planar defect energies can additionally be influenced by alloying additions. For example, at temperatures above about 850 °C, shearing of the γ' phase is mainly dominated by APB coupled $a/2\langle 110 \rangle$ superlattice dislocations in Ni based superalloys [30-32]. In Co based superalloys, such as Co-9Al-9W, shearing of the γ' phase is mainly dominated by SISFs coupled leading dislocation $a/3\langle 112 \rangle$ and trailing dislocation $a/6\langle 112 \rangle$. In Co-Ni-Al-W based superalloys, shearing of γ' precipitates was considered by a pair of

$a/2\langle 110 \rangle$ dislocations that leave APBs in their wake [4]. A high content of Ni in CoNi based superalloys usually decreases the APB energy. The main reason is Ni alloying influence partitioning coefficient of W and Al. The ratio of W/Al in γ' phase is higher, the APB and CSF is higher, see **Table 4**. For instance, in $L1_2$ Co_3Al , the APB and CSF energies are 53 mJ/m^2 and 5 mJ/m^2 , respectively. The values increase up to 293 mJ/m^2 and 287 mJ/m^2 in $L1_2$ $Co_3(Al,W)$. Titus et.al [4] concluded that the planar faults type transforms from SISFs to APBs with Ni concentration increasing, attributed into the discrepancy of SISF and APB formation energy. In single-phase $Co_3(Al,W)$, the SISF energy is smaller than APB energy and therefore shearing of the γ' phase leave SISFs in their wake. Nevertheless, SESF and SISF formation originates from chemical re-ordering process of CSF. Therefore, it is more reasonable to make discrepancy comparison between CSF and APB energy to discern favorable formation conditions of different planar fault types.

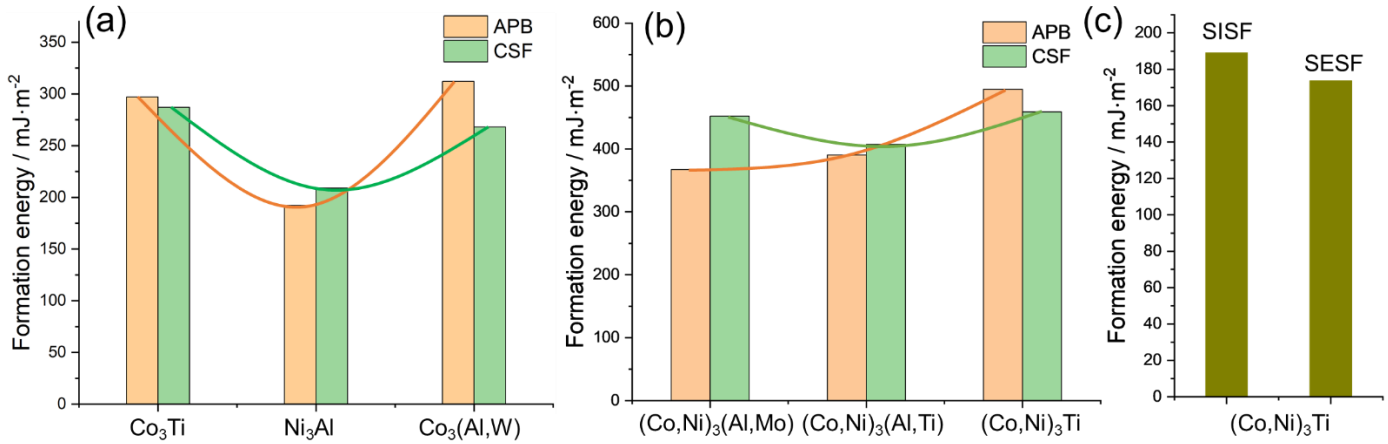


Fig. 11. (a) $E_{APB}^{(111)}$ and $E_{CSF}^{(111)}$ energies (mJ/m^2) of the $L1_2$ - Co_3Ti , $L1_2$ - $Co_3(Al,W)$ and $L1_2$ - Ni_3Al structures calculated by the DFT method in literatures [33-39]. (b) $E_{APB}^{(111)}$ and $E_{CSF}^{(111)}$ energies (mJ/m^2) of the $L1_2$ - $(Co_{0.5},Ni_{0.5})_3(Al_{0.5},Mo_{0.5})$, $L1_2$ - $(Co_{0.5},Ni_{0.5})_3(Al_{0.5},Ti_{0.5})$ and $L1_2$ - $(Co_{0.5},Ni_{0.5})_3Ti$ structures calculated by DFT method. (c) The discrepancy of the calculated $E_{SISF}^{(111)}$ and $E_{SESF}^{(111)}$ energies (mJ/m^2) of the $L1_2$ - $(Co_{0.5},Ni_{0.5})_3Ti$ structures by DFT method.

Fig. 11(a) and **Table 3** summarize literature values of APB and CSF formation energies on (111) crystal planes of three typical $L1_2$ compounds to expect in superalloys, $L1_2$ - Co_3Ti , $L1_2$ - $Co_3(Al,W)$ and $L1_2$ - Ni_3Al , calculated with the DFT method [33-39]. In the $L1_2$ ordered γ' - Ni_3Al phase, APB energy is usually lower than CSF formation energy and therefore, the shear mechanism in γ' - Ni_3Al phase is mainly by APB coupled $a/2\langle 110 \rangle$ matrix dislocation pairs at high temperature which has been proven by many experimental results [30, 31]. In the Co-Al-

W system, when the Co-based alloy is subjected to high-temperature plastic deformation, extended SISFs form in the γ' precipitates by dislocations shearing, as mentioned above. The CSF energy is 287 mJ/m² lower than APB energy, 293 mJ/m², that indicates CSF is much easier to be generated than APB in L1₂ Co₃(Al,W) structure. After chemical reordering, the CSF was transformed into the SISF. Titus et. al. [11] confirmed that the enrichment of Co, W and Ta in SISFs enables displacive-diffusive phase transformation, whereby the SISF assists the creation of the hexagonal Co₃W phase-(D0₁₉).

Table. 3. $E_{APB}^{(100)}$, $E_{APB}^{(111)}$, $E_{CSF}^{(111)}$, $E_{SISF}^{(111)}$ and $E_{SESF}^{(111)}$ energies (mJ/m²) of the L1₂-Co₃Ti, L1₂-Co₃(Ti,Mo), L1₂-Co₃(Al,Mo), L1₂-Co₃(Al,W), L1₂-Co₃Al, L1₂-Co₃W and L1₂-Ni₃Al phases. (^a Present DFT calculation at 0 K; ^b Experimental measurement at RT)

Structure	$E_{APB}^{(100)}$	$E_{APB}^{(111)}$	$E_{CSF}^{(111)}$	$E_{SISF}^{(111)}$	$E_{SESF}^{(111)}$
Co ₃ Ti ^a	308 ^[39]	312 ^[39]	268 ^[39]	147 ^[39]	86 ^[39]
Co ₃ (Ti,Mo) ^a	285 ^[39]	335 ^[39]	308 ^[39]	23 ^[39]	22 ^[39]
Ni ₃ Al ^a	95 ^[39]	192 ^[39]	209 ^[39]	70 ^[39]	185 ^[39]
Ni ₃ Al ^b	104±15 ^[38]	175±15 ^[38]	235±40 ^[38]	6±0.5 ^[38]	-
Co ₃ (Al,Mo) ^a	285 ^[37]	-	-	-	-
Co ₃ (Al,W) ^a	243 ^[34]	293 ^[35]	287 ^[35]	87 ^[35]	-
Co ₃ (Al,W) ^b	103 ^[33]	155±20 ^[33]	-	-	-
Co ₃ Al ^a	-14 ^[34]	-123 ^[36]	-184 ^[36]	-90 ^[36]	-
Co ₃ W ^a	111 ^[34]	399 ^[36]	523 ^[36]	-252 ^[36]	-
Co ₃ Ti ^{This work,a}	-	368	329	-	-
Co ₃ Al ^{This work,a}	-	53	5	-	-
(Co,Ni) ₃ Ti ^{This work,a}	-	495	458	189	174
(Co,Ni) ₃ (Al,Ti) ^{This work,a}	-	390	407	-	-
(Co,Ni) ₃ (Al,Mo) ^{This work,a}	-	367	452	-	-

There are less experimental research reports about planar defects in L1₂ ordered γ' -Co₃Ti phase due to its relatively lower phase stability compared with Ni₃Al and Co₃(Al,W). However, there are a large number of DFT simulation results to show CSF formation energy is lower than APB energy [39]. In addition, the SISF formation energy (147 mJ/m²) is higher than SESF formation energy (86 mJ/m²). Theoretically, the planar defect type in L1₂ ordered γ' -Co₃Ti phase should be SESF. Im et.al. [39] used DFT calculations to conclude there is increased likelihood of forming SESFs from CSFs by atomic reordering in the Co-12Ti-4Mo alloy. Therefore, in Co-based superalloys, the dislocation shearing of the γ' phase is mainly dominated by SFs. In Ni-based superalloys, the dislocation shearing mechanism of the γ' phase is mainly dominated by APBs.

In this study, planar faults type transforms from APBs towards SFs during precipitates shearing with Ti concentration increasing. Usually, Ti additions in superalloys, including Ni based, CoNi based and Co based superalloys, can increase APB energy [40, 41] by improving ordering of L1₂ structure. In principle, appropriate Ti addition is always beneficial for high temperature mechanical improvement by strengthening the γ' precipitates.

However, there is a gap on planar faults investigation with Ti content varying in alloys. The dislocations need overcome the initial energy barrier imposed by the CSF or APB which possesses nearest neighbor violations, resulting in a high planar fault energy. After that, the chemical reordering process facilitates transformation from high-energy faults (e.g., CSFs) into low-energy faults (e.g., SESFs or SISFs). In this work, we propose the discrepancy of APB and CSF energies is responsible for the transformation of planar faults. The final type of SFs depends on the difference of SESFs and SISFs energies.

By DFT calculations, shown in **Fig. 11(b)** and **Table 3**, the relative planar fault APB and CSF energies of the γ' phase in the alloys Ti-free, low-Ti and high-Ti can be inferred. The APB and CSF energies in the γ' phase were theoretically calculated for a variety of compositions ranging from L1₂ (Co_{0.5}Ni_{0.5})₃(Al_{0.5},Mo_{0.5}) to L1₂ (Co_{0.5}Ni_{0.5})₃(Al_{0.5},Ti_{0.5}) to L1₂ (Co_{0.5}Ni_{0.5})₃Ti representing Ti-free, low-Ti and high-Ti alloys, respectively. The APB energy is less than the CSF energy in Ti-free and low-Ti alloys, which could be the main reason for the prevalence of APBs in CoNi-base alloys with Ti-free and low-Ti additions. The Ti addition in superalloys contributes to the improvement of APB energy and therefore, we observed less APBs in low-Ti alloys than Ti-free alloys in crept samples shown in **Fig. 3**. In L1₂-(Co_{0.5}Ni_{0.5})₃Ti structure, the APB energy is higher than the CSF energy, which means that the shearing mode is mainly dominated by SFs. In addition, SESF energy (173 mJ/m²) is lower than SISF energy (189 mJ/m²) - proving that SESFs are more stable than SISFs in high-Ti superalloys.

A schematic of the γ' shearing mechanisms during high-temperature creep for the Ti-free, low-Ti, and high-Ti superalloys is shown in **Fig. 12**. The γ phase former element Co segregation and the γ' phase former elements depletion result in the softening of APBs. Therefore, the less APBs formation at high temperature is beneficial for creep resistance by low content of Ti additions. In high-Ti superalloys, SESFs become the main planar defects in the γ' phase but the segregation mechanism is different from APBs - Ni and Al are depleted and Co Ti, Mo and W are enriched to form a local phase (Co,Ni)₃(Ti,Mo,W).

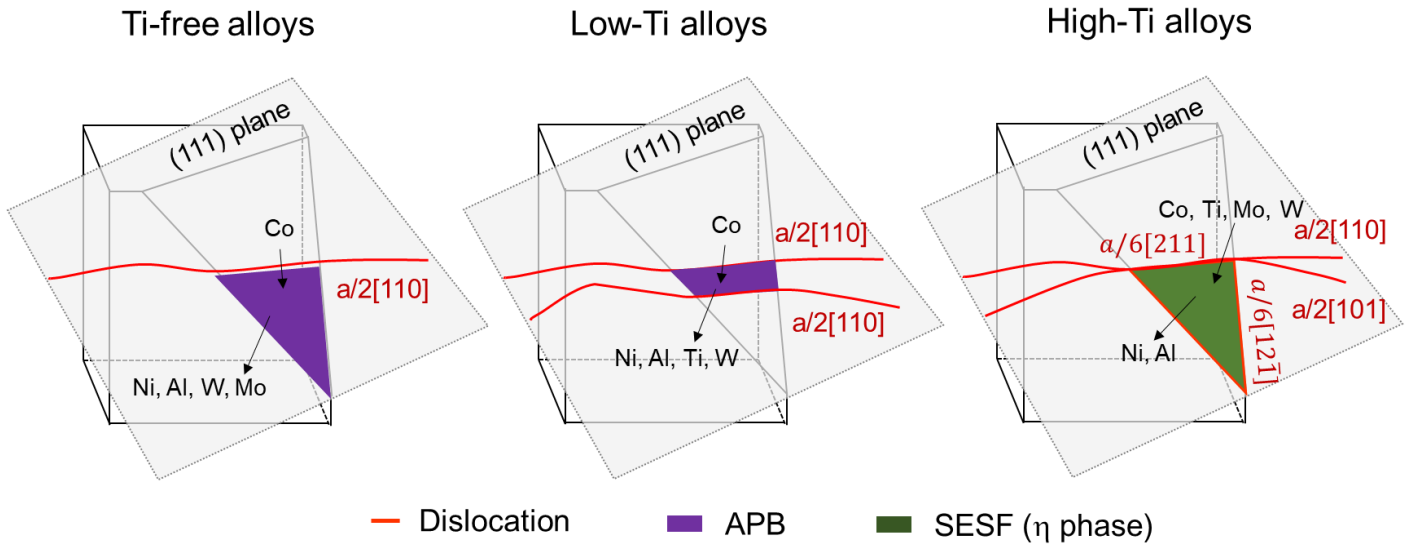


Fig. 12. Comparison of dislocation-precipitate shearing mechanisms during creep at high temperatures, *i.e.* 950 °C, in Ti-free, low-Ti and high-Ti CoNi based superalloys.

4.2 The γ' to η phase transformations

The concept of ‘reordering’, *i.e.* chemical segregation, has been suggested as a local, diffusion mediated process around faulted structures. In the Co based superalloys, chemical segregation directly occurred along SISFs. These nanoscale SISFs share the same crystal structure as do the equilibrium Co_3W -(D0_{19}) laths and via segregation tend to generate a local composition closer to the one of the bulk Co_3W phase. In addition, Smith et.al. [42] proposed that LPT occurred along SISFs in Ni based superalloys as well - the γ' phase transforms to χ phase (D0_{19}) in Ni based superalloy LSHR by chemical segregation. Yet, there is no evidence of a bulk, secondary minor phase with χ phase crystal structure present in commercial Ni-based superalloys.

Recent research has shown segregation of additional elements, such as Ti, Ta, Hf, and Nb, leading to a potent LPT strengthening effect by formation of η (D0_{24}) along superlattice extrinsic stacking faults (SESFs), as first observed by Smith et al. [7,13]. Particularly, the high Nb addition can induce triple LPT strengthening in SESFs (η , D0_{24}), SISFs (χ , D0_{19}) and microtwins’ boundary (χ , D0_{19}) [43]. Nevertheless, element Ti effect alone on LPT strengthening has never been reported yet. The main possible reason could be that Ti exhibits weak segregation behavior near the SESF when Ti is an example of such an alloying element. In **Fig. 8**, we found element segregation (Co, Ti, Mo and W) along SESFs shifting the local composition more towards the one of the η phase. Additionally, we investigated different Ti/Al ratio effect on microstructure in alloys. Above 8 at.% Ti in alloy, a high amount of lath η phases appeared in 10Ti and 12.5Ti alloys which directly proves the L1_2 Co-Ti and Ni-Ti

structures is unstable. Based on calculated structure formation energy of Co_3Ti , Ni_3Ti and Fe_3Ti by local-density total-energy approach [47], the L1_2 structured Co_3Ti is more stable than D0_{24} structure and the D0_{24} structure Ni_3Ti is more stable than L1_2 structure. When Ni is added to Co_3Ti , the L1_2 structured $(\text{Co,Ni})_3\text{Ti}$ become unstable and transforms into D0_{24} structure we think. Experiments presented L1_2 structure Ni_3Ti will transform into the stable D0_{24} structure during aging treatment at 600 °C [44, 45]. The corresponding mechanism observed in Ni_3Ti involving Shockley partial dislocations active for the transformation of fcc structure to the stacking sequence of the D0_{24} structure [44]. This result is identical to our present work. **Fig. 13(a)** presents SESF with Shockley partial dislocations exists within the L1_2 - γ' phase in 10Ti alloy and the bath η phase is alongside SESFs. **Fig. 13(b)** shows the Blackburn orientation relationship between γ and η by electron diffraction:

$$[110]\gamma' \parallel [2\bar{1}\bar{1}0]\eta$$

$$(\bar{1}11)\gamma' \parallel (0001)\eta$$

The Blackburn relationship accounts for the largest proportion for η precipitates formed in the solution stage. As a close-packed hexagonal ordered phase with the ABAC-type stacking sequence, the habit plane of η phase is the $(0001)\eta$ basal plane, which causes the assuming of the η - and γ -phase of a Blackburn orientation relationship because the closed packed planes match which are also the glide planes in the L1_2 structure. This supports that the phase transformation pathway takes place from L1_2 - γ' via local hcp-SESF to D0_{24} - η . Messé et.al. [46] reported the growth of the η phase requires long-range diffusion to produce the D0_{24} ordered structure. Therefore, the γ' to η phase transformation is mixed diffusive/displacive transformation.

However, the formation mechanisms of the lath η phase during aging and the local η phase (SESF) during creep are distinct. The diffusive/displacive transformation observed (lath η phase formation) during aging results from local compositional fluctuations, leading to local structural instability. The γ' phase undergoes continuous structural and compositional changes as it moves toward equilibrium, reflecting thermodynamic instability.

In contrast, the formation of the local η phase (SESF) during creep is driven by chemical segregation around a CISF, which causes the CISF to evolve into an SESF with chemical ordering. Initially, two Shockley superpartial dislocations shear the γ' phase, forming a CISF. These Shockley superpartial dislocations originate from the interaction of two $\langle 110 \rangle$ dislocations within the γ matrix. The process begins with a displacive transformation, followed by diffusional transformation along the CISF. As a result, during creep, the local η phase (SESF) thickens and transforms into a microtwin rather than developing into a lath η phase.

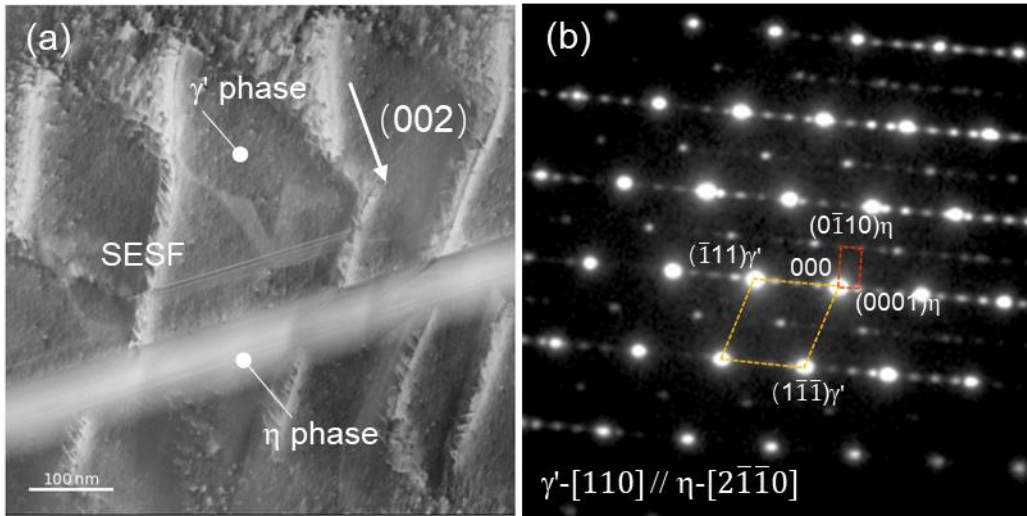


Fig. 13. (a) HAADF-STEM image of L_{12} - γ' phase, SESF and D_{024} - η lath in 10Ti alloy taken close to $[110]$ beam direction. (b) Selected area electron diffraction (SAED) pattern obtained from L_{12} - γ' phase and D_{024} - η phase.

Element segregation in small concentrations significantly reduces the SESF energy inside the γ' phase [48]. The reduction in SF energy assists the dislocation shearing process, whereby the critical stress for γ' shearing is well known to decrease linearly with decreasing SF or, more generally, planar defect energy [49]. This suggests that the diffusion of elements near SFs enables a quick decrease of the SF energy and therefore supports the leading dislocation to shear the γ' phase under a lower applied stress. Such a decrease in the stress required for γ' shearing is detrimental to high-temperature creep strength.

The γ' shearing with the formation of very stable coherent boundaries, such as SESFs, APBs, SISFs and microtwins, was thought to provide strengthening benefits. However, element segregation locally changes the properties of coherent boundaries, such as the disordered APB and ordered SESF regions. **Fig. 14** illustrates how segregation-assisted precipitate shearing occurs involving single $a/2 \langle 112 \rangle$ dislocation. Wetting phenomena proposed by Leroux et. al. [50] are structural changes of the intrinsic interface between two coexisting phases of matter when a third phase becomes more thermodynamically stable, which has been observed in-situ for the $L_{12} \rightarrow A1$ transformation near an APB. A more disordered APB region forms, which is able to locally soften the ordered γ' precipitates, is detrimental to high-temperature creep strength. The local phase transformation from the γ' phase to γ phase can be mainly attributed to the supersaturation of γ forming elements near the LPD. Subsequently, the APB formation will also help to expand the γ region by the wetting effect during the high-temperature creep process.

The ordered local η phase SESFs formation could be beneficial for precipitate hardening. However, segregation declined the SESF energy significantly which allows more $a/2 \langle 110 \rangle$ dislocations to choose to shear γ' phases not climbing over it. Moreover, the SESFs are 'embryo' for creep twins which usually makes big contribution for creep strain. Malte Lenz et.al [3] also summarized thickening of microtwins contributes much bigger creep strain compared with planar faults, such as SESFs, SISFs and APB. The microtwinning shearing accounts for the majority (73%-96% contribution) of the total plastic strain both within the secondary and third creep stages [5]. In addition, the dislocation pile-up events often occur at the twin boundaries. These dislocations pile-ups can eventually cause stress concentrations which can lead to crack nucleation and propagation along the twin-parent interfaces. This mechanism causes brittle fracture when microtwins appear.

The shearing of precipitates can also influence the rafting process directly. This point can be verified by results in alloy 0Ti. The majority of dislocations are able to shear γ' particles easily generating low energy APB faults instead of circumventing the γ' cubes by climb. Dislocation climb is directly associated with diffusion of atoms based on the pipe diffusion along the dislocation line. The onset of cutting of γ' -particles is assumed to be the microstructural state when the minimum creep rate is observed. Dislocation climb does not significantly contribute to the overall creep strain but it can influence the creep rate by changing not only the density and spatial arrangement of dislocations (dislocation networks) but also the rafting of γ' -cubes. Therefore, in order to avoid the shearing of precipitates at high temperature with low stress, the appropriate Ti concentration (we suggest $0 < \text{Ti/Al ratio} < 1$) should be employed in superalloys.

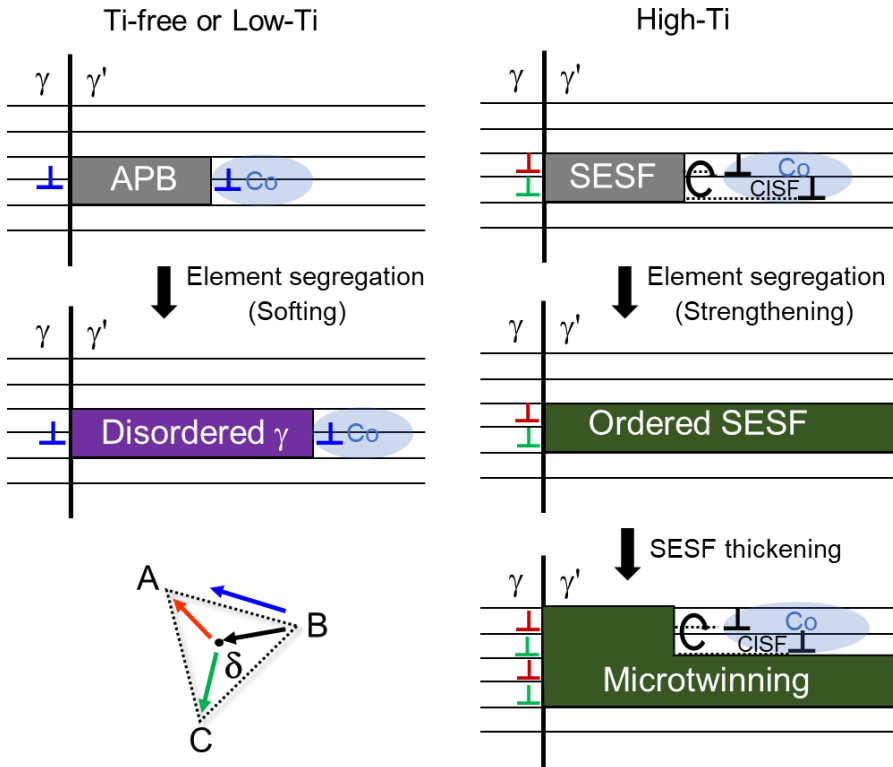


Fig.14. Summary of Ti content dependent fault shearing modes and local phase transformation (LPT) effects.

5. Summary

In this study, we studied shearing mechanisms in the γ' precipitates in CoNi based superalloys with different Ti contents during creep at 950 °C under low applied stress. The preferred shearing mode in γ' precipitates is highly likely to be affected by the APB and CSF energies which decides the planar fault type reside in the γ' precipitates.

In Ti-free or low-Ti superalloys, the APB energy is lower than the CSF energy. Therefore, shearing of the γ' phase mainly occurs by superlattice dislocations $a/2\langle 110 \rangle$ leaving a disordered APB region in their wake and local phase transformation towards γ phase is caused by elemental segregation at the APBs on both (111) and (001) crystal planes. In high-Ti superalloys, the APB energy is higher than the CSF energy. The shearing mode with APB formation becomes unfavourable and the γ' shearing takes place by movement of partial $a/6\langle 121 \rangle$ dislocations generating high energy CSFs. Subsequently, those CSFs are transformed into low energy SESF by elemental reordering accompanying elemental segregation at high temperature. The segregation at SESFs was shown to be a kind of local phase transformation strengthening by forming ordered η phases inside of the γ' precipitates. According to literatures, the η -type SESFs formation is able to inhibit creep twinning formation, to

some extent, but not completely. With creep strain and time going, e.g., later (secondary and tertiary) creep stages, the η -type SESFs will become thicker and transformed into microtwins which is different with aging process, i.e., the η -type SESFs will transform into lath η phase by thickening. The microtwinning can contribute significant to overall creep strain, higher than other defects (APBs, SISFs and SESFs). To enhance creep resistance, it is crucial to consider the factors that influence the formation and thickening of microtwins. While η -type SESFs can effectively inhibit the thickening of microtwins, they cannot completely prevent their formation. To fully prevent the formation of creep-induced microtwins, a lower Ti content should be employed.

References

- [1] R.C. Reed, *The superalloys: fundamentals and applications*. Cambridge university press, (2008).
- [2] Eggeler, Y. M., Müller, J., Titus, M. S., Suzuki, A., Pollock, T. M., & Spiecker, E. (2016). Planar defect formation in the γ' phase during high temperature creep in single crystal CoNi-base superalloys. *Acta Materialia*, 113, 335-349.
- [3] Lenz, M., Eggeler, Y. M., Müller, J., Zenk, C. H., Volz, N., Wollgramm, P., ... & Spiecker, E. (2019). Tension/Compression asymmetry of a creep deformed single crystal Co-base superalloy. *Acta Materialia*, 166, 597-610.
- [4] Titus, M. S., Eggeler, Y. M., Suzuki, A., & Pollock, T. M. (2015). Creep-induced planar defects in L12-containing Co-and CoNi-base single-crystal superalloys. *Acta Materialia*, 82, 530-539.
- [5] Barba, D., Alabort, E., Pedrazzini, S., Collins, D. M., Wilkinson, A. J., Bagot, P. A. J., ... & Reed, R. C. (2017). On the microtwinning mechanism in a single crystal superalloy. *Acta Materialia*, 135, 314-329.
- [6] L. Kovarik, R.R. Unocic, J. Li, P. Sarosi, C. Shen, Y. Wang, M.J. Mills, Microtwinning and other shearing mechanisms at intermediate temperatures in Ni-based superalloys. *Prog. Mater. Sci.* 54(6) (2009) 839-873.
- [7] T.M. Smith Jr, *Orientation and alloying effects on creep strength in Ni-based superalloys* (Doctoral dissertation, The Ohio State University), (2016).
- [8] N. Tsuno, S. Shimabayashi, K. Kakehi, C.M.F. Rae, R.C. Reed. Tension/Compression asymmetry in yield and creep strengths of Ni-based superalloys. In *Superalloys 2008, Proceedings of the International Symposium on Superalloys*, pages 433-442, 2008.
- [9] F. Leon Cazares, *On the plastic deformation behaviour of nickel-based superalloys: low cycle fatigue and stress orientation effects* (Doctoral dissertation, University of Cambridge), (2020).
- [10] T.M. Smith, B.D. Esser, N. Antolin, A. Carlsson, R.E.A. Williams, A. Wessman, M.J. Mills, Phase transformation strengthening of high-temperature superalloys. *Nat. Commun.* 7(1) (2016) 1-7.

- [11] Titus, M. S., Rhein, R. K., Wells, P. B., Dodge, P. C., Viswanathan, G. B., Mills, M. J., ... & Pollock, T. M. (2016). Solute segregation and deviation from bulk thermodynamics at nanoscale crystalline defects. *Science advances*, 2(12), e1601796.
- [12] Feng, L., Lv, D., Rhein, R. K., Goiri, J. G., Titus, M. S., Van der Ven, A., ... & Wang, Y. (2018). Shearing of γ' particles in Co-base and Co-Ni-base superalloys. *Acta Materialia*, 161, 99-109.
- [13] Smith, T. M., Esser, B. D., Antolin, N., Viswanathan, G. B., Hanlon, T., Wessman, A., ... & Mills, M. J. (2015). Segregation and η phase formation along stacking faults during creep at intermediate temperatures in a Ni-based superalloy. *Acta Materialia*, 100, 19-31.
- [14] Lilensten, L., Antonov, S., Gault, B., Tin, S., & Kontis, P. (2021). Enhanced creep performance in a polycrystalline superalloy driven by atomic-scale phase transformation along planar faults. *Acta Materialia*, 202, 232-242.
- [15] P.E. Blöchl, Projector augmented-wave method, *Physical Review B* 50(24) (1994) 17953-17979.
- [16] G. Kresse, J. Furthmüller, Efficiency of ab-initio total energy calculations for metals and semiconductors using a plane-wave basis set, *Computational Materials Science* 6(1) (1996) 15-50.
- [17] A. Zunger, S.H. Wei, L.G. Ferreira, J.E. Bernard, Special quasirandom structures, *Physical Review Letters* 65(3) (1990) 353-356.
- [18] J.P. Perdew, K. Burke, M. Ernzerhof, Generalized Gradient Approximation Made Simple, *Physical Review Letters* 77(18) (1996) 3865-3868.
- [19] H.J. Monkhorst, J.D. Pack, Special points for Brillouin-zone integrations, *Physical Review B* 13(12) (1976) 5188-5192.
- [20] Liang, Z., Stark, A., & Pyczak, F. (2024). Extreme high lattice-misfit superalloys with regular cubic L12 particles and excellent creep resistance. arXiv preprint arXiv:2405.05851.
- [21] T. Yokokawa, H. Harada, K. Kawagishi, T. Kobayashi, M. Yuyama, Y. Takata, Advanced alloy design program and improvement of sixth-generation Ni-base single crystal superalloy TMS-238. In *Superalloys 2020: Proceedings of the 14th International Symposium on Superalloys* (pp. 122-130). Springer International Publishing.
- [22] T. Murakumo, T. Kobayashi, Y. Koizumi, H. Harada, Creep behaviour of Ni-base single-crystal superalloys with various γ' volume fraction. *Acta Mater.* 52(12) (2004) 3737-3744.
- [23] J.X. Zhang, J.C. Wang, H. Harada, Y. Koizumi, The effect of lattice misfit on the dislocation motion in superalloys during high-temperature low-stress creep. *Acta mater.* 53(17) (2005) 4623-4633.
- [24] J.X. Zhang, T. Murakumo, H. Harada, Y. Koizumi, Dependence of creep strength on the interfacial dislocations in a fourth generation SC superalloy TMS-138. *Scripta Mater.* 48(3) (2003) 287-293.
- [25] Kolbe, M. (2001). The high temperature decrease of the critical resolved shear stress in nickel-base superalloys. *Materials Science and Engineering: A*, 319, 383-387.

- [26] Karpstein, N., Lenz, M., Bezold, A., Wu, M., Neumeier, S., & Spiecker, E. (2023). Reliable identification of the complex or superlattice nature of intrinsic and extrinsic stacking faults in the L12 phase by high-resolution imaging. *Acta Materialia*, 260, 119284.
- [27] Freund, L. P., Messé, O. M., Barnard, J. S., Göken, M., Neumeier, S., & Rae, C. M. (2017). Segregation assisted microtwinning during creep of a polycrystalline L12-hardened Co-base superalloy. *Acta Materialia*, 123, 295-304.
- [28] He, J., Zenk, C. H., Zhou, X., Neumeier, S., Raabe, D., Gault, B., & Makineni, S. K. (2020). On the atomic solute diffusional mechanisms during compressive creep deformation of a Co-Al-W-Ta single crystal superalloy. *Acta Materialia*, 184, 86-99.
- [29] Lu, S., Antonov, S., Li, L., Liu, C., Zhang, X., Zheng, Y., ... & Feng, Q. (2020). Atomic structure and elemental segregation behavior of creep defects in a Co-Al-W-based single crystal superalloys under high temperature and low stress. *Acta Materialia*, 190, 16-28.
- [30] Morris, D. G., & Morris, M. A. (1990). Antiphase domain boundaries and their importance for dislocation behaviour in Ni₃Al based alloys. *Philosophical Magazine A*, 61(3), 469-491.
- [31] Hazzledine, P. M., Yoo, M. H., & Sun, Y. Q. (1989). The geometry of glide in Ni₃Al at temperatures above the flow stress peak. *Acta Metallurgica*, 37(12), 3235-3244.
- [32] Barba, D., Smith, T. M., Miao, J., Mills, M. J., & Reed, R. C. (2018). Segregation-assisted plasticity in Ni-based superalloys. *Metallurgical and Materials Transactions A*, 49, 4173-4185.
- [33] N.L. Okamoto, T. Oohashi, H. Adachi, K. Kishida, H. Inui, P. Veyssi re, Plastic deformation of polycrystals of Co₃(Al,W) with the L12 structure. *Philos. Mag.* 91(28) (2011) 3667-3684.
- [34] J.E. Saal, C. Wolverton, Energetics of antiphase boundaries in L1₂ Co₃(Al,W)-based superalloys. *Acta Mater.* 103 (2016) 57-62.
- [35] K.V. Vamsi, S. Karthikeyan, Yield anomaly in L12 Co₃Al_xW_{1-x} vis-a-vis Ni₃Al, *Scripta Mater.* 130 (2017) 269-273
- [36] H. Hasan, P. Milkvik, P.D. Haynes, V.A. Vorontsov, Generalised stacking fault energy of Ni-Al and Co-Al-W superalloys: Density-functional theory calculations. *Materialia*, 9 (2020) 100555.
- [37] W.Y. Wang, F. Xue, Y. Zhang, S.L. Shang, Y. Wang, K. A. Darling, , Z.K. Liu, Atomic and electronic basis for solutes strengthened (010) anti-phase boundary of L12 Co₃(Al,TM): A comprehensive first-principles study. *Acta Mater.* 145 (2018) 30-40.
- [38] H.P. Karnthaler, E.T. M hlbacher, C. Rentenberger, The influence of the fault energies on the anomalous mechanical behaviour of Ni₃Al alloys. *Acta Mater.* 44(2) (1996) 547-560.
- [39] H.J. Im, S. Lee, W.S. Choi, S.K. Makineni, D. Raabe, W. S. Ko, P.P. Choi, Effects of Mo on the mechanical behavior of γ/γ' -strengthened Co-Ti-based alloys. *Acta Mater.* 197 (2020) 69-80.

- [40] Chandran, M., & Sondhi, S. K. (2011). First-principle calculation of APB energy in Ni-based binary and ternary alloys. *Modelling and Simulation in Materials Science and Engineering*, 19(2), 025008.
- [41] Wang, W. Y., Xue, F., Zhang, Y., Shang, S. L., Wang, Y., Darling, K. A., ... & Liu, Z. K. (2018). Atomic and electronic basis for solutes strengthened (010) anti-phase boundary of L12 Co₃(Al, TM): a comprehensive first-principles study. *Acta Materialia*, 145, 30-40.
- [42] Smith, T. M., Good, B. S., Gabb, T. P., Esser, B. D., Egan, A. J., Evans, L. J., ... & Mills, M. J. (2019). Effect of stacking fault segregation and local phase transformations on creep strength in Ni-base superalloys. *Acta Materialia*, 172, 55-65.
- [43] Egan, A. J., Xue, F., Rao, Y., Sparks, G., Marquis, E., Ghazisaeidi, M., ... & Mills, M. J. (2022). Local phase transformation strengthening at Microtwin boundaries in nickel-based superalloys. *Acta Materialia*, 238, 118206.
- [44] Lambrigger, M., Calderon, H. A., & Kostorz, G. (1992). Phase Transformation to the Stable D024 Structure in Ni-11.8 at.% Ti/Phasenumwandlung zur stabilen D024-Struktur in Ni-11, 8 At.-% Ti. *International Journal of Materials Research*, 83(8), 624-629.
- [45] Al-Kassab, T., Kompatscher, M., Kirchheim, R., Kostorz, G., & Schönfeld, B. (2014). Phase decomposition and ordering in Ni-11.3 at.% Ti studied with atom probe tomography. *Micron*, 64, 45-51.
- [46] Messé, O. M., Barnard, J. S., Pickering, E. J., Midgley, P. A., & Rae, C. M. F. (2014). On the precipitation of delta phase in ALLVAC® 718Plus. *Philosophical Magazine*, 94(10), 1132-1152.
- [47] Xu, J. H., Lin, W., & Freeman, A. J. (1993). Electronic structure and phase stability of A3Ti (A= Fe, Co, Ni, and Cu). *Physical Review B*, 48(7), 4276.
- [48] M. S. Titus, A. Mottura, G. B. Viswanathan, A. Suzuki, M. J. Mills, T. M. Pollock, High resolution energy dispersive spectroscopy mapping of planar defects in L12-containing Co-base superalloys. *Acta Mater.* 89, 423–437 (2015).
- [49] J. P. Hirth, Thermodynamics of stacking faults. *Metall. Trans.* 1, 2367–2374 (1970).
- [50] Leroux, C., Loiseau, A., Cadeville, M. C., Broddin, D., & Van Tendeloo, G. (1990). Order-disorder transformation in Co₃₀Pt₇₀ alloy: evidence of wetting from the antiphase boundaries. *Journal of Physics: Condensed Matter*, 2(15), 3479.

High-Ti inducing η -phase transformation and creep-twinning in CoNi-based superalloys

Zhida Liang^{1,4*}, Jing Zhang^{2,*}, Li Wang³, Florian Pyczak¹

1. Institute of Materials Physics, Helmholtz-Zentrum Hereon, Max-Planck-Strasse 1, Geesthacht 21502, Germany
2. Key Laboratory of MEMS of Ministry of Education, School of Integrated Circuits, Southeast University, Nanjing, China
3. State Key Laboratory of Powder Metallurgy, Central South university, 410083 Changsha, China
4. Laboratory for Electron Microscopy, Karlsruhe Institute of Technology, Engesserstraße 7, Karlsruhe 76131, Germany

*Corresponding author: zhida.liang@outlook.com (Zhida Liang), jizh@seu.edu.cn (Jing Zhang)

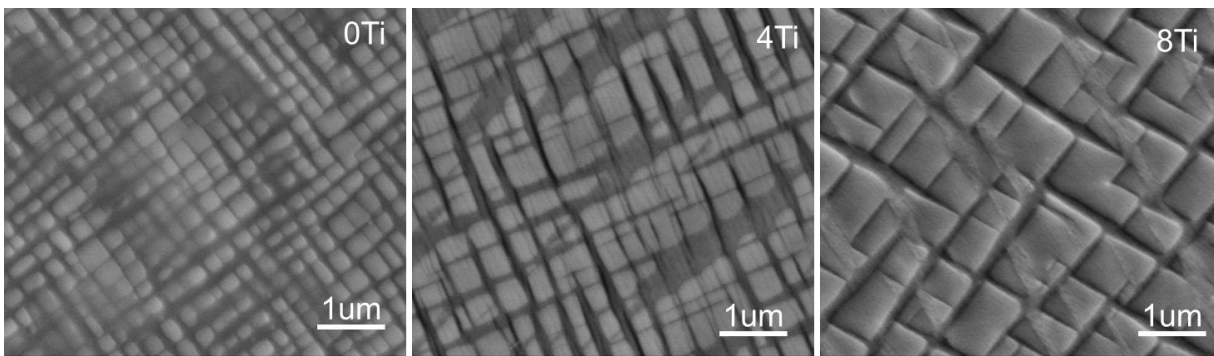


Fig. S1. The BSE images of γ'/γ binary phases in alloys 0Ti, 4Ti and 8Ti, respectively.

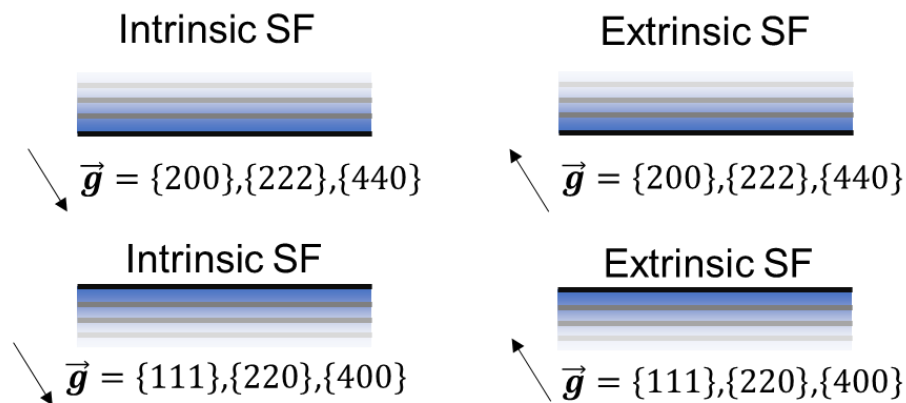
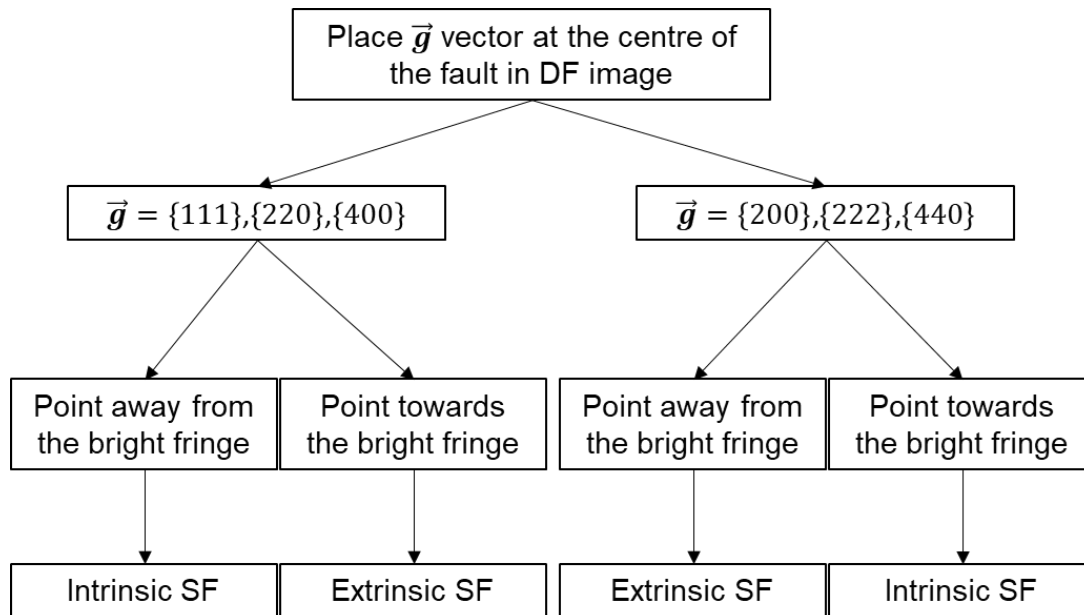


Fig. S2. Systematic flow chart showing the criterion for extrinsic and intrinsic SF nature determination [51-54]. The basic procedure is to put the \vec{g} vector of dark field (DF) image in the center of the stacking fault, as indicated by the dashed arrow in the middle of the stacking fault, and determine whether the \vec{g} vector points away or towards the outermost bright fringe of the stacking fault.

[51] P. B. Hirsch, A. Howie, R. Nicholson, D. Pashley, M. Whelan, Electron microscopy of thin crystals, Butterworths, Washington DC, 1965.

[52] J. W. Edington, Practical Electron Microscopy in Materials Science., Voan Nostrand, New York, 1975.

[53] D. B. Williams, C. B. Carter, The transmission electron microscope, Springer, New York, 1996.

[54] Wu, X. (2017). Elementary deformation processes during low temperature and high stress creep of Ni-base single crystal superalloys.

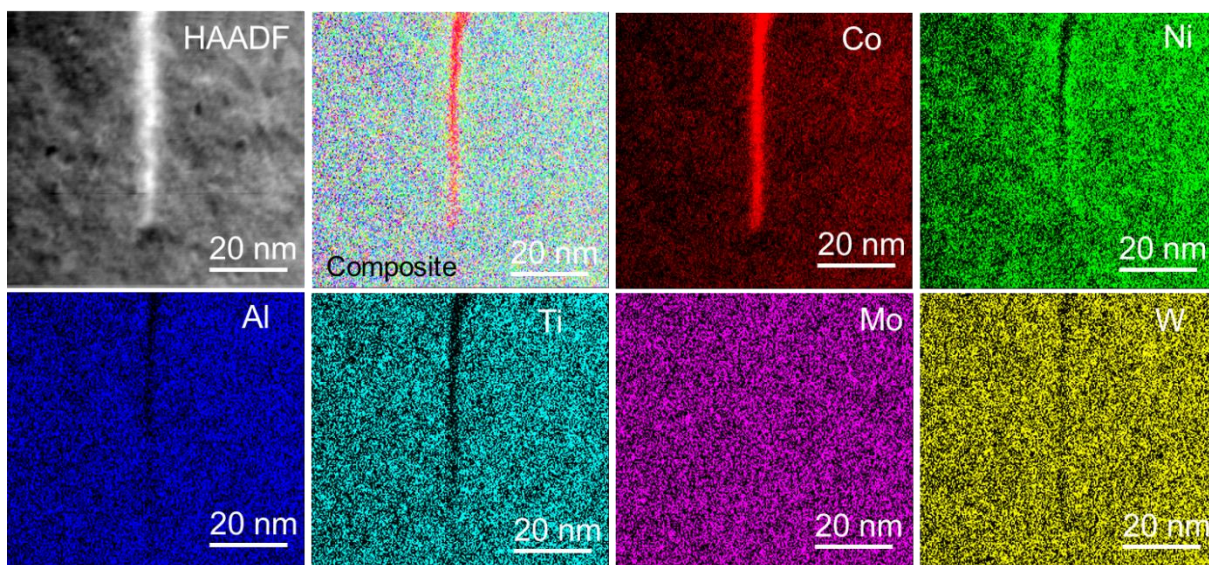


Fig. S2. Chemical fluctuations analysis along APB on (001) planes inside a γ' precipitate in alloy 4Ti. (a) HAADF-STEM image for the γ' precipitate with APBs in [001] beam direction. (b) The composite chemical map of elements Co, Ni, Al, Ti, Mo and W. (d)-(h) Net intensity elemental maps of elements Co, Ni, Al, Ti, Mo and W.

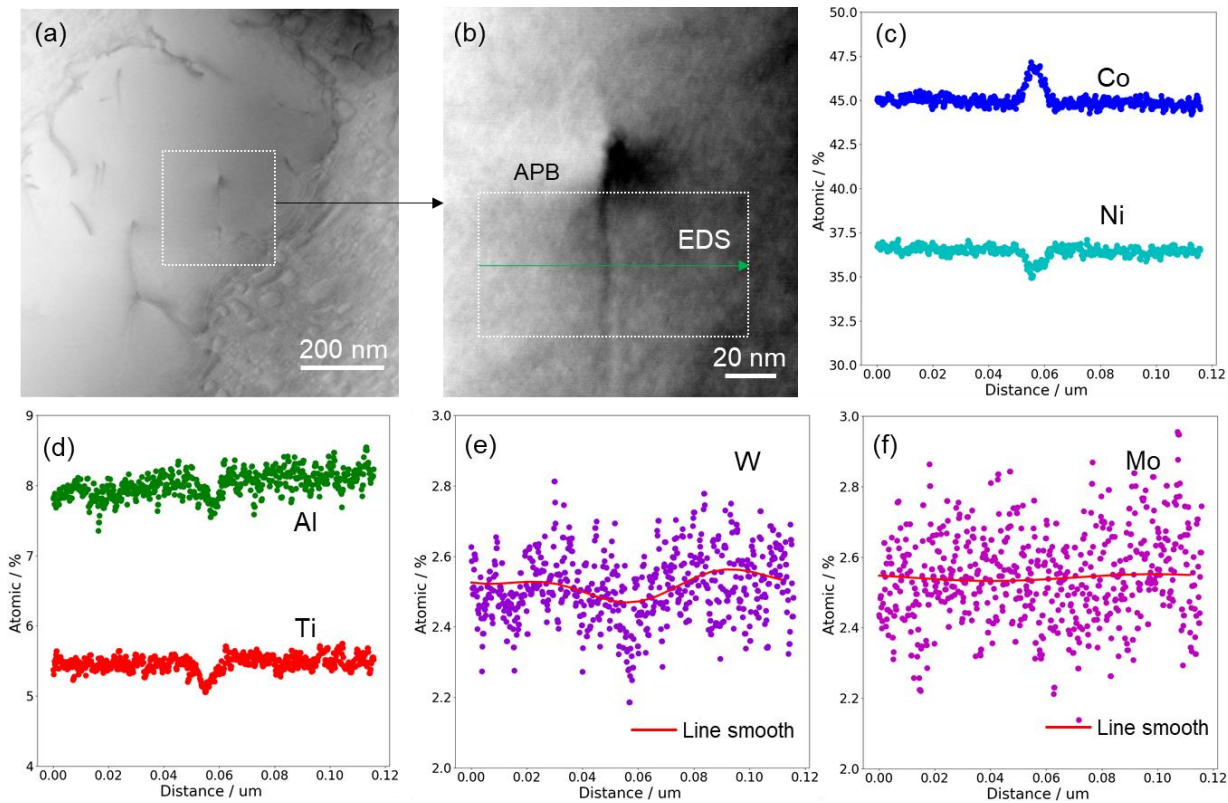


Fig. S3. Chemical fluctuations analysis along APB on (111) planes inside a γ' precipitate in alloy 4Ti. (a) HAADF-STEM image for the γ' precipitate with APBs in [011] beam direction. (b) The magnified image of white rectangular in (a). (c) The composite chemical map of elements Co, Ni, Al, Mo and W. (d)-(h) Net intensity elemental maps of elements Co, Ni, Al, Mo and W. (i) and (j) A integrated EDS line scan across the APB from (c).

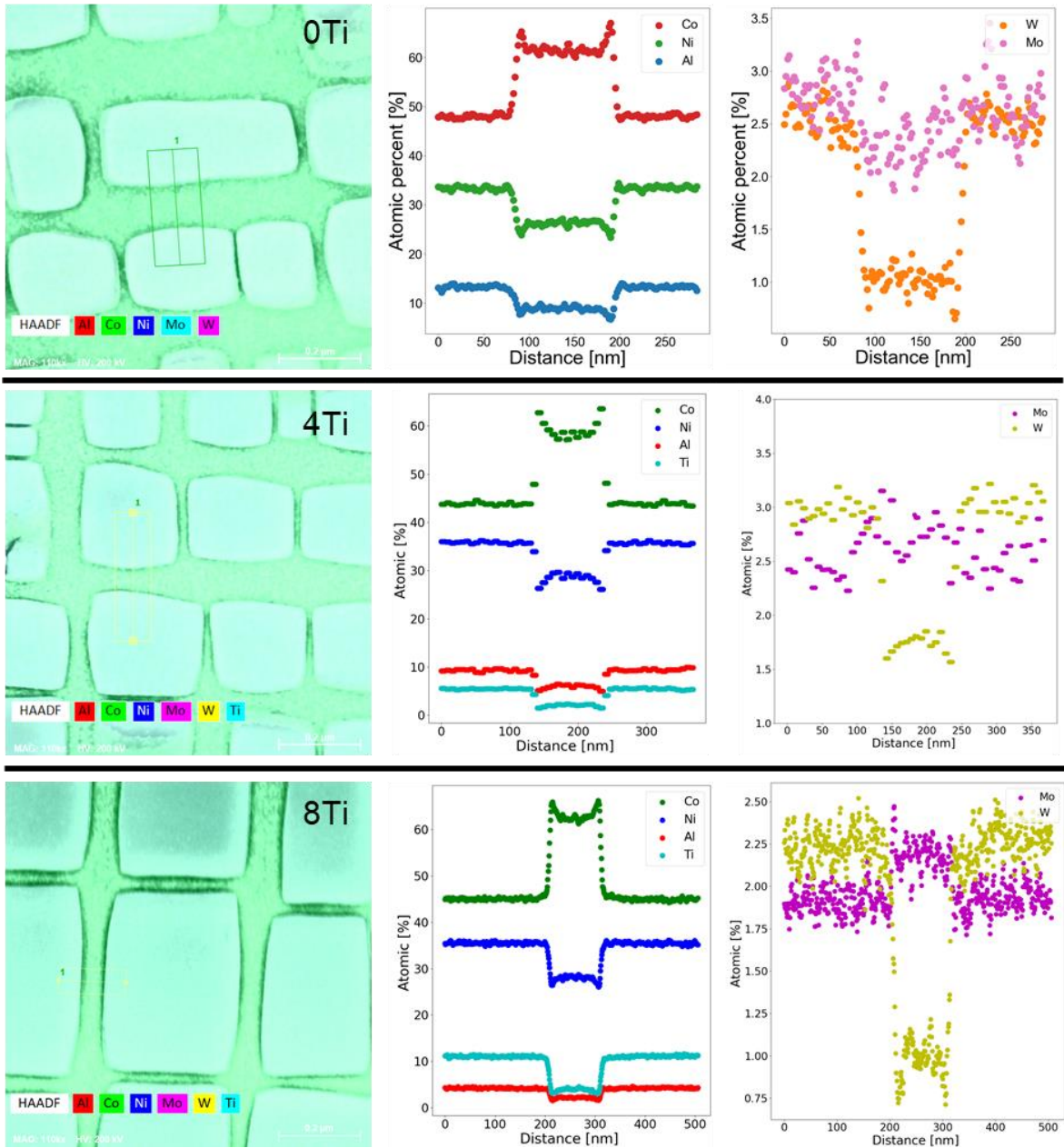


Fig. S4. Element distribution in the γ' and γ two phases of alloys 0Ti, 4Ti and 8Ti. In alloy 0Ti, only Co prefers to partition into γ matrix while Ni, Al, Mo and W partition into γ' phase. In alloy 4Ti, Co prefers to partition into γ matrix as well and Ni, Al, Ti and W partition into γ' phase but Mo has a balanced distribution in the γ' and γ two phases. In alloy 8Ti, Co and Mo prefer to partition into γ matrix and Ni, Al, Ti and W partition into γ' phase. With changing Ti content in CoNi-based superalloys, the Mo changed from γ matrix former to γ' phase former.

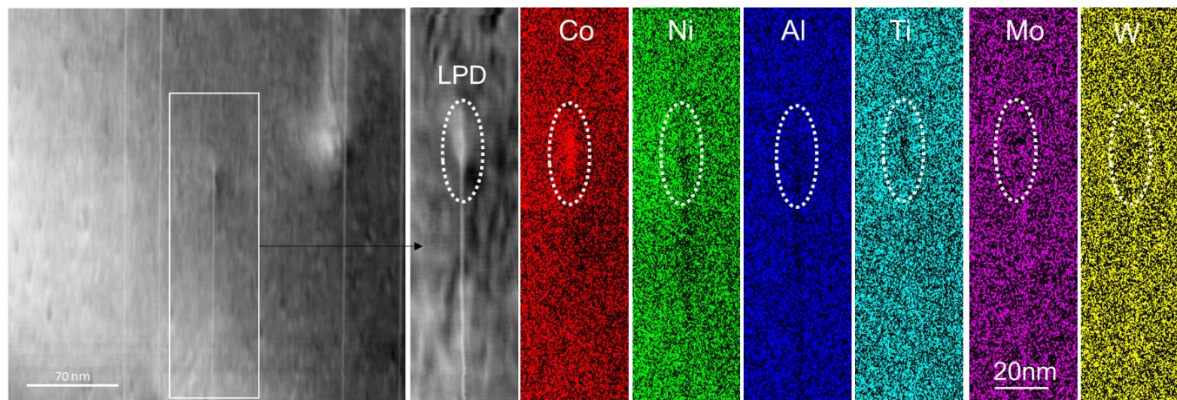


Fig. S5. The HAADF-STEM and EDS maps. Co segregate but Ni, Al and Ti deplete into leading partial dislocation (LPD).

Table S1. The crystallography information for the prototype η phase (Ni_3Ti).

Formula	Space group	Elements	Wyck.	Atom coordinates			Cell parameters
				x	y	z	
Ni_3Ti (η , D024)	$P6_3/mmc$ (194)	Ni	$6h$	0.16667	0.33333	0.25	$a=b=5.1 \text{ \AA}$
		Ni	$6g$	0.5	0	0	$c=8.3 \text{ \AA}$
		Ti	$2d$	0.33333	0.66667	0.75	$\alpha=\beta=90^\circ$
		Ti	$2a$	0	0	0	$\gamma=120^\circ$